Research Square

Preprints are preliminary reports that have not undergone peer review.
They should not be considered conclusive, used to inform clinical practice,
or referenced by the media as validated information.

Immunomimetic Bioengineered Vesicles Targeting TGF-β and PD-L1 Enhance Antitumor Efficacy through Pyroptosis-Driven Trained Immunity Coordinated with Adaptive Immunity

Yanbing Ma

MolecularImmunology@imbcams.com.cn

Institute of Medical Biology, Chinese Academy of Medical Sciences & Peking Union Medical College

Peng Zheng

Laboratory of Molecular Immunology, Institute of Medical Biology, Chinese Academy of Medical Sciences & Peking Union Medical College.

Sihang Bao

School of Life Sciences, Yunnan University

Tong Yu

Laboratory of Molecular Immunology, Institute of Medical Biology, Chinese Academy of Medical Sciences & Peking Union Medical College.

Ying Yang

Institute of Medical Biology, Chinese Academy of Medical Sciences & Peking Union Medical College

Xin Yin

Laboratory of Molecular Immunology, Institute of Medical Biology, Chinese Academy of Medical Sciences & Peking Union Medical College.

Yu Liu

State Key Laboratory of Proteomics, Beijing Proteome Research Center, National Center for Protein Sciences-Beijing (PHOENIX Center), Beijing Institute of Lifeomics, Beijing, 102206, China.

Yiru Tian

Institute of Medical Biology, Chinese Academy of Medical Sciences & Peking Union Medical College

Xiang Zhang

Institute of Medical Biology, Chinese Academy of Medical Sciences & Peking Union Medical College

Shuqin Li

Institute of Medical Biology, Chinese Academy of Medical Sciences & Peking Union Medical College

Qiong Long

Laboratory of Molecular Immunology, Institute of Medical Biology, Chinese Academy of Medical Sciences & Peking Union Medical College.

Hongmei Bai

Institute of Medical Biology, Chinese Academy of Medical Sciences & Peking Union Medical College

Xu Yang

Institute of Medical Biology, Chinese Academy of Medical Sciences & Peking Union Medical College

Article

Keywords:

Posted Date: November 24th, 2026

DOI: https://doi.org/10.21203/rs.3.rs-11663191/v1

License: This work is licensed under a Creative Commons Attribution 4.0 International License.
Read Full License

Additional Declarations: There is **NO** Competing Interest.

Immunomimetic Bioengineered Vesicles Targeting TGF-β and PD-L1 Enhance Antitumor Efficacy through Pyroptosis-Driven Trained Immunity Coordinated with Adaptive Immunity

*Peng Zheng[1,4], Sihang Bao[1,2,4], Tong Yu[1,4], Ying Yang[1], Xin Yin[1], Yu Liu[1], Yiru Tian[1], Xiang Zhang[1,3], Shuqin Li[1], Qiong Long[1], Hongmei Bai[1], Xu Yang[1], Yanbing Ma[1,2,3]**

[1]Laboratory of Molecular Immunology, Institute of Medical Biology, Chinese Academy of Medical Sciences & Peking Union Medical College, Kunming 650118, China

[2]School of Life Sciences, Yunnan University, Kunming 650091, China

[3]Kunming Medical University, Kunming 650500, China

[4]These authors contributed equally: Peng Zheng, Sihang Bao, Tong Yu.

* Correspondence: MolecularImmunology@imbcams.com.cn

Abstract

Solid tumors exhibit profound resistance to immune checkpoint blockade (ICB) driven by a synergistic network of TGF-β-induced physical barriers and PD-L1-mediated adaptive immune resistance. Here, we report a rationally engineered immunomimetic bioengineered vesicle, TP-IBV, constructed on a low-endotoxin *ClearColi* chassis. TP-IBV co-displays a TGFβRII decoy receptor and a uPA-responsive PD-L1 nanobody (nb) to achieve spatiotemporally controlled immunomodulation. TP-IBV monotherapy achieved a 14.2% cure rate in the MC38 model and outperformed conventional antibody combinations in the 4T1 model. Mechanistically, TP-IBV neutralizes TGF-β to inhibit CAF activation and ECM collagen deposition, thereby dismantling the physical barrier for $CD8^+$ T cell infiltration. Concurrently, the localized uPA-responsive release of PD-L1 nb alleviates T cell exhaustion, effectively converting "cold" tumors into "hot" ones. Beyond remodeling the local TME, TP-IBV induces immunogenic cell death and triggers a dual-pyroptosis cascade, characterized by GSDMD-mediated initiation and $CD8^+$/NK cell-derived granzyme B-mediated GSDME cleavage. The resulting massive release of tumor antigens and DAMPs, such as HMGB1, not only constitutes a potent *in situ* vaccine but also provides a systemic feedback signal to the bone marrow, amplifying the baseline central trained immunity established by the IBV chassis. This study reveals a functional link between local immunogenic cell death and central trained immunity, providing a programmable and translational nanoplatform to overcome multi-layered immunosuppression in solid tumors.

Keywords: Cancer immunotherapy; Bacterial vesicles; Central trained immunity; Pyroptosis; TGF-β; PD-L1

Introduction

Immune checkpoint inhibitor (ICI) therapy has significantly advanced the management of advanced cancers. However, clinical response rates remain limited,

with only about 20% to 30% of patients benefiting[1, 2, 3]. This persistent resistance largely stems from the complex, multi-layered defense mechanisms established by solid tumors. At the physical level, transforming growth factor-β (TGF-β) activates tumor-associated fibroblasts (TAFs), driving abnormal extracellular matrix (ECM) deposition and remodeling. This creates a dense fibrotic barrier that restricts the infiltration of both therapeutic agents and immune cells[4, 5]. Biochemically, TGF-β serves as a central regulator of immunosuppression, directly inhibiting the cytotoxic activity of $CD8^+$ T cells and natural killer (NK) cells while promoting the differentiation and recruitment of regulatory T cells (Tregs) [6, 7, 8, 9]. Concurrently, tumor cells upregulate programmed death ligand-1 (PD-L1), which interacts with the PD-1 receptor on infiltrating T cells, leading to inhibitory signaling and T-cell exhaustion [6]. Recent research indicates that these two pathways are interconnected: TGF-β signaling can upregulate PD-L1 expression through the SMAD protein complex, and the PD-1/PD-L1 interaction further sensitizes T cells to TGF-β-mediated suppression, establishing a robust, synergistic immunosuppressive network [10, 11, 12].

To overcome the limitations of single-pathway inhibition, strategies targeting both TGF-β and PD-L1 have gained momentum [10, 13, 14, 15, 16]. However, systemic administration of monoclonal antibodies faces severe challenges, including poor spatiotemporal coordination, limited tissue penetration, and the risk of systemic toxicity [17]. Nanotechnology-based drug delivery systems offer a potential solution. Conventional platforms such as liposomes, polymer micelles, and inorganic nanoparticles possess distinct advantages in drug solubilization, pharmacokinetic control, and passive tumor targeting via the enhanced permeability and retention effect [18, 19, 20, 21]. Despite these merits, most of these systems lack intrinsic immunostimulatory capacity and the ability to achieve stimuli-responsive, coordinated release of multiple payloads. This limitation hinders their ability to remodel the immunosuppressive tumor microenvironment fully. Thus, identifying a programmable delivery carrier that combines natural adjuvant activity with precise engineering capabilities is highly desirable.

Given these requirements, bacterial membrane vesicles (BMVs) have emerged as attractive candidates due to their inherent pathogen-associated molecular patterns (PAMPs), ease of engineering, and favorable biocompatibility [22, 23, 24, 25, 26]. However, traditional BMVs exhibit strong endotoxin (lipopolysaccharide, LPS) activity, which triggers severe systemic inflammatory responses at high doses, severely limiting their clinical translation [27, 28, 29, 30]. To address this, we utilized an engineered, attenuated *ClearColi* strain that fails to mature LPS, significantly reducing the activation of the Toll-like receptor 4 (TLR4)/myeloid differentiation factor 2 (MD2) complex [31]. The resulting immunomimetic bioengineered vesicle (IBV) platform retains the natural adjuvant properties of the bacterial membrane while ensuring systemic safety, thereby paving the way for clinical translation.

Beyond conventional innate immune activation, the concept of trained immunity has recently reshaped our understanding of host defense [32, 33]. Inducers such as β-

glucan, Bacillus Calmette-Guérin (BCG), and yeast-derived whole β-glucan particles (WGP) can enhance the antitumor activity of monocytes and macrophages through epigenetic and metabolic reprogramming, sustaining long-term immune surveillance [34, 35, 36, 37, 38, 39, 40, 41]. However, most current trained immunity research focuses on exogenous microbial or adjuvant stimulation, while endogenous inducers (such as oxidized LDL) are primarily studied in autoimmune contexts [42, 43, 44, 45]. Reprogramming myeloid cells in the bone marrow, which underlies central trained immunity, is crucial for generating functionally reprogrammed immune cells from hematopoietic precursors [33, 46]. This presents a novel perspective for systemic antitumor immunity, which remains underexplored in the context of engineered nanomedicines.

Pyroptosis, a highly pro-inflammatory form of immunogenic cell death (ICD), has garnered attention for its role in remodeling the tumor immune microenvironment[47, 48]. Protease-mediated cleavage of Gasdermin family proteins increases membrane permeability, leading to the massive release of damage-associated molecular patterns (DAMPs), such as high mobility group box 1 (HMGB1) and ATP [49]. These released DAMPs act in concert with tumor antigens to function as a potent *in situ* vaccine [50]. However, it is uncertain whether the DAMPs released during tumor cell pyroptosis can provide feedback to the bone marrow and act as molecular adjuvants to enhance central trained immunity. The mechanism linking local *in situ* pyroptosis with central trained immunity has not yet been experimentally established.

To simultaneously address TGF-β-mediated immunosuppression and the negative feedback of the PD-1/PD-L1 axis, we rationally designed a bifunctional immunomodulatory vesicle, TP-IBV, using synthetic biology. The platform comprises two main components: First, we anchored the extracellular domain of TGF-βRII to the vesicle surface as a decoy receptor (T-IBV module) to target and neutralize TGF-β. Second, to overcome the limitations of conventional PD-L1 antibodies, we concealed a small PD-L1 nanobody (~15 kDa) on the vesicle surface via a urokinase-type plasminogen activator (uPA)-responsive peptide switch, enabling precise spatiotemporal release specifically at the uPA-rich tumor invasion front.

Our data demonstrate that *ClearColi*-derived IBV induces systemic trained immunity to suppress tumor growth. The T-IBV module broadly binds TGF-β1, TGF-β2, and TGF-β3 *in vitro*. In both MC38 and 4T1 tumor-bearing mice, T-IBV significantly increases the proportion of antigen-specific $CD8^+$ T cells in the TME. Furthermore, the integrated bifunctional TP-IBV exhibits superior antitumor efficacy compared to monofunctional vesicles, free antibodies, and the physical co-administration of both in cold tumor models. Mechanistically, TP-IBV not only inhibits CAF activation and collagen deposition and attenuates $CD8^+$ T-cell exhaustion, but also drives GSDMD/GSDME-dependent tumor cell pyroptosis, resulting in massive DAMP release. We further confirmed that pyroptosis-derived HMGB1 potently induces trained immunity. Notably, when GSDMD was

pharmacologically inhibited *in vivo*, BMDMs showed significantly reduced IL-6 and TNF-α secretion upon restimulation with LPS, Pam3CSK4, or tumor lysates, attenuating central trained immunity and subsequently compromising antitumor efficacy.

This study shows that DAMPs released during TP-IBV-induced *in situ* pyroptosis, with HMGB1 as a key mediator, signal retrogradely to the bone marrow. This feedback loop amplifies the baseline central trained immunity induced by the vesicle itself, thereby establishing long-lasting systemic antitumor immunity. By linking endogenous pyroptosis to central trained immunity, our work extends the functional scope of pyroptosis in antitumor immunity beyond adaptive T-cell activation to include systemic myeloid cell reprogramming.

Results

Engineering, physicochemical characterization, and validation of the broad-spectrum TGF-β binding capacity of T-IBV

To precisely reverse TGF-β-mediated immune suppression in the tumor microenvironment (TME), we designed a genetic engineering strategy to fuse the extracellular domain of mouse TGFβRII to the C-terminus of the *E. coli* membrane-anchoring protein ClyA via a flexible linker peptide ($(GGGGS)_4$). This design was intended to create immunomimetic vesicles that surface-display TGFβRII and directly intercept TGF-β (T-IBV). We achieved efficient expression of the fusion protein and vesicle self-assembly in the endotoxin-free engineered strain *ClearColi*, successfully constructing T-IBV **(Figure 1A)**. Sodium Dodecyl Sulfate-Polyacrylamide Gel Electrophoresis (SDS-PAGE) and Western blotting analyses confirmed the successful anchoring and specific expression of the target protein (ClyA-TGFβRII) on T-IBVs **(Figure 1B–C)**. Next, physical characterization showed that the hydrodynamic diameter of T-IBV was approximately 100 nm, with a uniform particle-size distribution, consistent with unmodified vesicles (IBV); under transmission electron microscopy (TEM), both exhibited typical, intact spherical vesicle structures **(Figure 1D–G)**. In stability assessments, after storage at different temperatures (–20 °C, 4 °C, 25 °C) for 14 days, multiple freeze-thaw cycles, and incubation in medium containing 10% fetal bovine serum (FBS) at 37 °C, the particle size and polydispersity index (PDI) of T-IBV showed no significant fluctuations, supporting its colloidal stability and suitability for in vivo circulation and tumor enrichment **(Figure 1H)**.

In terms of biosafety, the *ClearColi* engineered strain, due to deletion of seven specific genes, cannot convert precursor lipid IVA into mature LPS. Furthermore, it lacks two of the six acetyl chains required for recognition by the TLR4–MD2 complex, thereby blocking TLR4 pathway activation [31] **(Figure 1I)**. Quantitative endotoxin testing showed that endotoxin levels in IBV and T-IBV derived from *ClearColi* were reduced by approximately 191.1-fold and 157.7-fold, respectively, compared with vesicles derived from wild-type *E. coli* **(Figure 1J)**, reducing the risks associated with systemic administration and supporting their suitability as a safer bacterial carrier. To further validate function, we verified the biological activity of the surface-displayed receptors through coating experiments **(Figure 1K)**. Enzyme-linked immunosorbent assay (ELISA) results showed that the T-IBV-coated surface could bind the three major immunosuppressive subtypes—TGF-β1, TGF-β2, and TGF-β3—with high affinity in a concentration-dependent manner, whereas the control group IBV showed no significant binding signal **(Figure 1L–N)**. This confirms that the surface-displayed TGFβRII retains its native conformation and supports its role as a

"molecular sponge" to capture TGF-β in the TME. Overall, these data demonstrate that we have successfully engineered T-IBV with high stability, excellent biosafety, and broad-spectrum TGF-β neutralizing capacity.

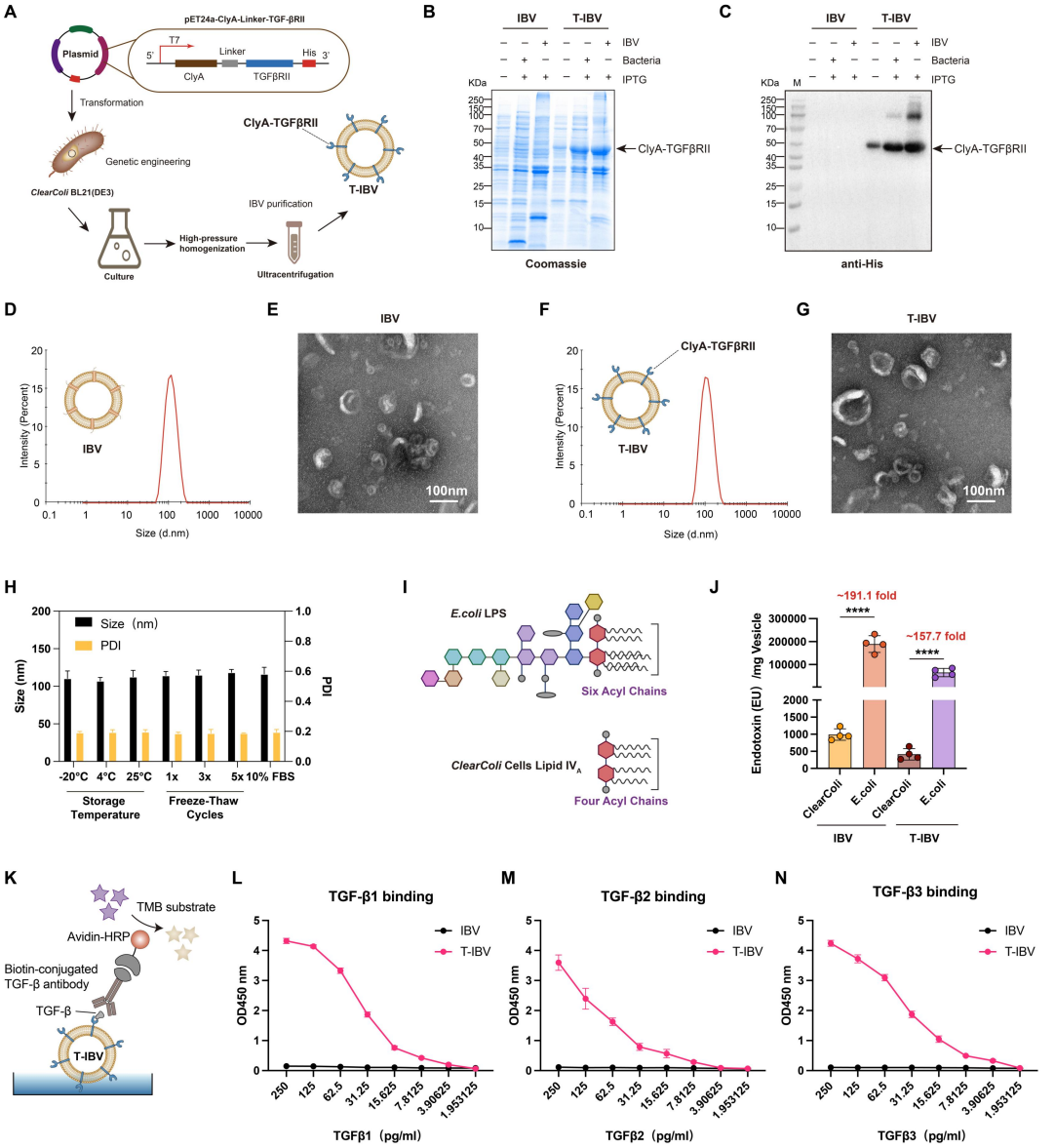

Figure 1. Preparation and Characterization of T-IBV. (A) Schematic diagram of the T-IBV plasmid construction, preparation, and purification process; (B) SDS-PAGE with Coomassie staining to identify TGF-βRII on T-IBV; (C) Western blotting analysis of TGF-βRII expression on T-IBV using an anti-His antibody; (D) Particle size distribution characteristics of IBV determined by DLS; (E) Representative TEM image of purified IBV. (F) Particle size distribution characteristics of T-IBV determined by DLS; (G) Representative TEM image of purified T-IBV. (H) Stability assessment of T-IBV under different storage conditions, freeze-thaw cycles, and after 2 weeks in 10% FBS (n=3); (I) Schematic comparison of the structures of E. coli LPS and the lipid IVA substitute from *ClearColi*. (J) Detection of endotoxin content (EU) per μg of IBV and T-IBV derived from wild-type *E. coli* and *ClearColi*; endotoxin was quantified using the LAL assay (n=4); (K) Schematic illustration of the principle of ELISA-based detection of TGF-β binding to T-IBV at different concentrations; (L–N) Binding assays of TGF-β1 (L), TGF-β2 (M), or TGF-β3 (N) at different

concentrations to T-IBV coated on plates. Serial dilutions of TGF-β1, TGF-β2, or TGF-β3 were incubated with T-IBV on coated plates to assess binding, which was detected by enzyme-linked immunosorbent assay (ELISA) (n = 3 technical replicates). IBV served as a control, and optical densities (OD) were read at 450 nm. Data are shown as the mean ± standard deviation (SD). Statistical significance was determined using one-way analysis of variance (ANOVA) followed by Tukey's multiple comparisons (J). *p < 0.05, **p < 0.01, ***p < 0.001, ****p < 0.0001; ns, not significant.

ClearColi-IBV Retains Adjuvant Activity That Induces Systemic Trained Immunity and Effectively Inhibits Tumor Growth

After successfully constructing and producing endotoxin-free engineered vesicles, we further investigated whether attenuated IBV derived from *ClearColi* retains the capacity to reprogram the innate immune system over the long term, specifically to induce trained immunity. Trained immunity is characterized by a significantly enhanced immune response generated by innate immune cells upon secondary inflammatory stimulation after epigenetic and metabolic reprogramming following initial stimulation [46]. To validate this activity, we established an *in vitro* trained immunity model **(Figure 2A, E)**. *In vitro* results indicated that both IBV and T-IBV, regardless of whether they were derived from wild-type *E. coli* or *ClearColi*, significantly enhanced the response of bone marrow-derived dendritic cells (BMDCs) and macrophages (BMDMs) to LPS restimulation following initial stimulation, elution, and a six-day resting period **(Figure 2A, E)**. This enhancement was evidenced by a substantial increase in IL-6, IL-1β, and TNF-α secretion **(Figure 2B–D, F–H)**. Notably, we observed no statistically significant difference in the ability to induce trained immunity between vesicles derived from *ClearColi* and those from wild-type strains. These findings suggest that, although the engineered attenuation strategy eliminated the risk of endotoxin (LPS)-induced acute inflammation, the adjuvant activity of other pathogen-associated molecular patterns (PAMPs), such as flagellin and peptidoglycan, within the vesicles remained effective in activating trained immunity.

To determine whether IBV-induced trained immunity could be sustainably established *in vivo*, we administered a single intravenous injection of IBV, followed by LPS restimulation via intraperitoneal injection on day 30 post-injection **(Figure 2I)**. Serological assays showed that mice pretreated with IBV 30 days earlier had significantly higher serum levels of IL-6, IL-1β, and TNF-α after restimulation than the PBS control group **(Figure 2J)**. These results provide conclusive evidence that IBV induces long-lasting innate immune memory *in vivo*, rather than a transient inflammatory response. We then traced the anatomical localization of the systemic trained immune response **(Figure 2K)**. We isolated immune cells from the bone marrow, spleen, lymph nodes, and lungs and restimulated them to assess the anatomical distribution of trained immunity. Bone marrow-derived macrophages (BMDMs) exhibited strong features of trained immunity upon restimulation, confirming that IBV effectively acts on hematopoietic progenitor cells to establish central trained immunity **(Figure 2L)**. Similarly, mixed populations of lymphocytes and myeloid cells from the spleen and lymph nodes exhibited enhanced cytokine secretion **(Figure 2M–N)**, indicating the establishment of trained immunity in peripheral secondary lymphoid organs. In contrast, lung tissue did not show a significant increase in IL-6 and IL-1β secretion following restimulation **(Figure 2O)**. After characterizing the anatomical features of IBV-induced trained immunity, we

further investigated whether this long-lasting innate immune memory could be converted into a functional antitumor effect. To exclude acute inflammation and rigorously evaluate the memory effect, we observed a 30-day rest period after intravenous IBV injection before inoculating the MC38 colon cancer model **(Figure 2P)**. The tumor growth curves indicated that in mice pre-trained with IBV, both the rate of tumor growth and the final tumor volume were significantly suppressed **(Figure 2Q)**. These data show that, despite the significant reduction in endotoxin levels, IBV retains its capacity to induce trained immunity and, consequently, delays tumor progression *in vivo*.

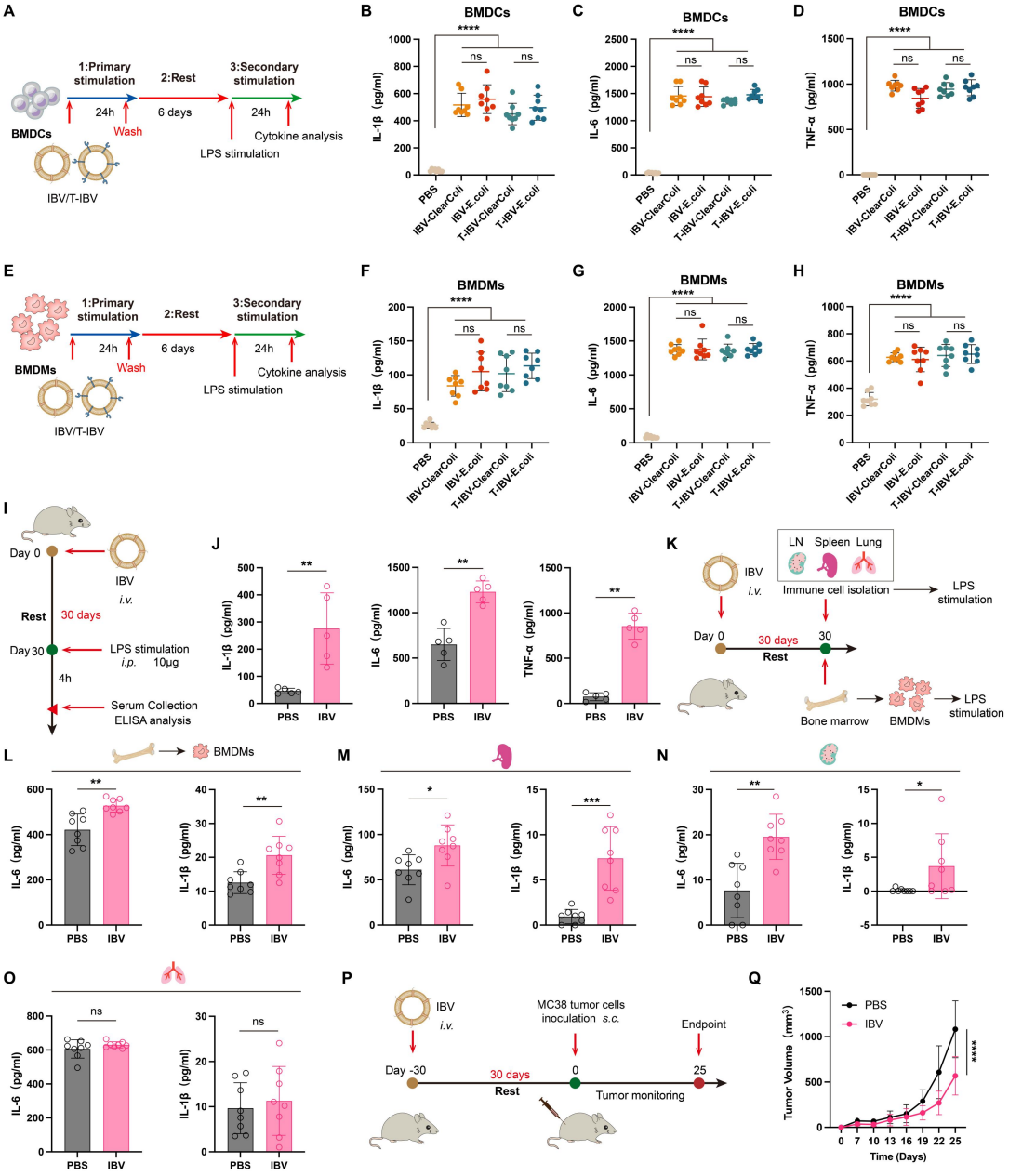

Figure 2. *ClearColi*-IBV induces trained immunity and effectively inhibits tumor growth. (A) Schematic diagram of the in vitro induction of trained immunity in BMDCs using IBV/T-IBV derived from *ClearColi* and *E. coli*; (B–D) After training BMDCs with IBV/T-IBV derived from *ClearColi* and *E. coli*, followed by a 6-day rest period, cytokine levels of IL-1β (B), IL-6 (C), and TNF-α (D) were measured by

ELISA 24 hours after restimulation with LPS (n = 8); (E) Schematic diagram of the in vitro immunization process for BMDMs induced by IBV/T-IBV derived from *ClearColi* and *E. coli*; (F–H) BMDMs trained with IBV/T-IBV derived from *ClearColi* and *E. coli*; after a 6-day rest period, they were re-stimulated with LPS, and cytokine levels of IL-1β (F), IL-6 (G), and TNF-α (H) were measured by ELISA 24 hours later (n = 8); (I) Schematic diagram illustrating the in vivo assessment of the IBV-induced trained immunity process; (J) Following intravenous injection of IBV, serum was collected 30 days later and 4 hours after intraperitoneal stimulation with LPS; cytokine levels of IL-1β, IL-6, and TNF-α were measured by ELISA (n=5); (K) Schematic diagram illustrating the evaluation of IBV-induced peripheral and central trained immunity. Thirty days after intravenous injection of IBV, lymph nodes (LN), spleen, and lung tissues were collected, and immune cell suspensions were isolated. These cells were re-stimulated with LPS in vitro for 24 hours, and cytokine levels were measured. Concurrently, 30 days after injection, bone marrow cells were isolated and differentiated into BMDMs in vitro; cytokine levels were then measured 24 hours after LPS restimulation. (L) Following intravenous injection of IBV, 30 days later, BMDMs were isolated from differentiated bone marrow cells; cytokine levels (IL-6 and IL-1β) were measured 24 hours after in vitro restimulation with LPS (n=8); (M) A single-cell suspension was prepared from isolated spleen cells; cytokine levels (IL-6 and IL-1β) were measured 24 hours after in vitro restimulation with LPS (n=8); (N) After isolating immune cells from lymph nodes (LN), cytokine levels of IL-6 and IL-1β were measured 24 hours after in vitro LPS restimulation (n=8); (O) After isolating immune cells from the lungs, cytokine levels of IL-6 and IL-1β were measured 24 hours after in vitro LPS restimulation (n=8); (P) Schematic diagram illustrating the tumor suppression of MC38 by IBV-induced trained immunity; (Q) Tumor growth curves in mice following intravenous injection of IBV, followed by inoculation with MC38 tumor cells 30 days later (n=8). Data are shown as the mean ± standard deviation (SD). Statistical significance was determined using one-way analysis of variance (ANOVA) followed by Tukey's multiple comparisons (B-D, F-H) or unpaired two-tailed Student's t-tests (J, L-O), and a two-way ANOVA (Q). *$p < 0.05$, **$p < 0.01$, ***$p < 0.001$, ****$p < 0.0001$; ns, not significant.

T-IBV's Exceptional Immunological Safety and Moderate Innate Immune Activation Capacity

To validate the safety rationale in a preclinical setting, we conducted an *in vivo* dose-escalation toxicity evaluation in healthy mice. Animals were administered different doses of *ClearColi* T-IBV (50, 100, 200, and 500 μg) or 200 μg of wild-type *E. coli* T-IBV **(Figure 3A)**. Survival data showed that all mice in the *ClearColi* T-IBV dose groups survived, whereas the survival rate in the *E. coli* T-IBV group was only 37.5% **(Figure 3B)**. Regarding body weight, the *E. coli* group exhibited a sharp decline as early as 2 hours post-injection, which persisted until 72 hours. In contrast, no significant body weight changes were observed in any *ClearColi* group **(Figure 3C)**. Further analysis of cytokine secretion kinetics during the acute phase showed that *E. coli* T-IBV triggered a severe inflammatory response as early as 2 hours post-injection. Peak IL-6 and TNF-α levels far exceeded those observed with the highest

dose of 500 μg *ClearColi* T-IBV **(Figure 3D–E)**, and inflammatory mediators such as IL-1β and IFN-γ also increased sharply **(Figure 3F–G)**. In contrast, the cytokine increase induced by *ClearColi* T-IBV followed a distinct transient pattern, with levels returning to baseline within 12 hours. This self-limiting kinetic profile indicates acute, controllable immunostimulation rather than persistent chronic inflammation. This brief innate activation phase is a prerequisite for establishing durable trained immunity without eliciting systemic pathology, aligning with our observation that IBV effectively primes long-term innate immune memory upon exogenous re-stimulation **(Figure 2).** Hematoxylin-Eosin (H&E) staining **(Figure S1, Supplementary Information)** provided additional visual evidence of tissue damage. In the *E. coli* T-IBV group, we observed marked thickening of the pulmonary stroma, destruction of alveolar structures, and significant immune cell infiltration within the liver parenchyma. By comparison, even after administration of a high dose of 500 μg *ClearColi* T-IBV, the mouse lungs and liver remained healthy and intact. Taken together, these data establish the exceptional biosafety of the *ClearColi* T-IBV platform and support its moderate innate immune activation as a safety foundation for subsequent high-dose and repeated-dose administration strategies.

TGF-β receptor-mediated active targeting has been shown to prolong T-IBV retention within the TME and inhibit tumor growth.

Effective targeting and sustained presence at the tumor site are considered essential for T-IBV to achieve its TGF-β-neutralizing function. To clarify the clinical relevance of the T-IBV active targeting strategy, we systematically analyzed TGF-β ligand expression patterns in solid tumors using data from The Cancer Genome Atlas (TCGA) database **(Figure S2, Supplementary Information)**. In both colorectal cancer **(Figure S2A, Supplementary Information)** and breast cancer **(Figure S2B, Supplementary Information)**, TGF-β ligand expression was significantly higher in tumor regions than in normal tissues. Paired-sample analysis revealed subtype-specific differences. In colorectal cancer, TGF-β1 and TGF-β2 were significantly upregulated **(Figure S2C, Supplementary Information)**, while in breast cancer, TGF-β1 and TGF-β3 showed more pronounced tumor-specific overexpression **(Figure S2D, Supplementary Information)**. TGF-β1, as a highly abundant inhibitory factor in the tumor microenvironment, showed a highly statistically significant increase in both solid tumors. This provides a broad and abundant pool of binding ligands for the TGFβRII receptor displayed on the surface of T-IBV.

Building on this clinical background, we performed *in vivo* tracing experiments using DiL-labeled T-IBV in MC38 tumor-bearing mice **(Figure 3H)**. *In vivo* imaging indicated that the fluorescence signal of unmodified IBV diminished rapidly at the tumor site. In contrast, T-IBV accumulated more extensively in the tumor region, with a strong fluorescence signal that remained stable for up to 120 hours post-injection **(Fig. 3I–J)**. This tumor-targeting capability likely reflects the enhanced permeation and retention (EPR) effect and TGFβRII-mediated binding to TGF-β ligands in the tumor microenvironment. Fluorescence imaging of *ex vivo* organs **(Figure S3A–B, Supplementary Information)** further supported this observation. Over time, the fluorescence signal of T-IBV in non-target organs such as the liver and lungs decreased significantly **(Figure S3B, Supplementary Information)**. Confocal microscopy also revealed extensive colocalization of DiL-labeled T-IBV with endogenous TGF-β in tumor tissue sections **(Figure 3K)**, visually confirming that T-IBV resides within the tumor. Given these targeting and binding characteristics, we evaluated the preliminary antitumor efficacy of T-IBV in the MC38 colorectal cancer

model; the treatment regimen involved three intravenous injections every 3 days **(Figure 3L)**. Tumor growth curves showed that T-IBV's inhibitory effect on MC38 tumors was dose-dependent within the 50–200 μg range, as both tumor growth rate and final volume decreased significantly with increasing dose **(Figure 3M–N)**. However, tumor growth did not differ significantly between the 100 μg and 200 μg dose groups. This finding suggests that the antitumor effect of this carrier may reach a plateau at approximately 100 μg. Given that the antitumor efficacy plateaued at 100 μg with no significant additional benefit at higher doses, and to minimize systemic exposure while maximizing the safety margin, we selected 100 μg as the optimal dose for subsequent mechanistic studies and combination therapy.

In summary, T-IBV, through genetic engineering-based attenuation technology and active targeting of the TGF-β receptor, has been shown to achieve long-term retention and functional binding within a tumor microenvironment characterized by high TGF-β concentrations, while maintaining low systemic toxicity. Colorectal cancer progression was effectively inhibited in a dose-dependent manner, providing a solid experimental foundation for further investigation into the mechanisms by which T-IBV may reshape the immune microenvironment and for its potential use in combination therapy with immune checkpoint inhibitors.

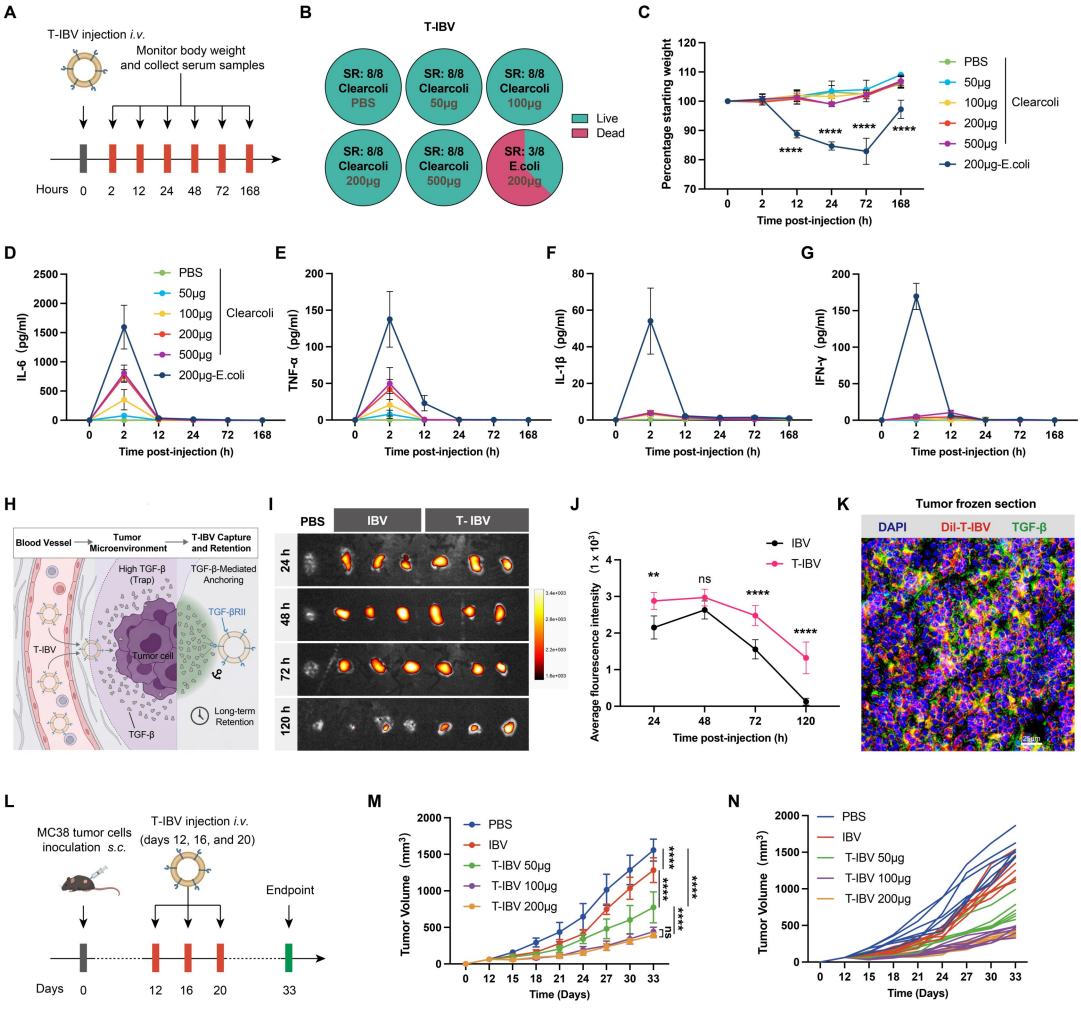

Figure 3. Evaluation of the safety and antitumor effects of T-IBV derived from *ClearColi*. (A) Schematic diagram of the *in vivo* safety evaluation process following a single intravenous injection of different doses of *ClearColi*-T-IBV (50 μg, 100 μg, 200 μg, 500 μg) and 200 μg of *E. coli* T-IBV; (B) Survival rate (SR) of mice after injection of specified doses of *ClearColi*-T-IBV and *E. coli* T-IBV (n = 8); (C) Monitoring of body weight changes in mice following injection of specified doses of *ClearColi*-T-IBV and *E. coli* T-IBV (n = 8); (D – G) Monitoring of serum cytokine levels (IL-6, TNF-α, IL-1β, and IFN-γ) in mice at different time points following injection of specified doses of *ClearColi*-T-IBV and *E. coli* T-IBV (n = 3); (H) Schematic illustration of the mechanism by which T-IBV, after intravenous injection, actively targets tumors and prolongs its retention time by binding to TGF-β, which is highly expressed within the tumor; (I) Representative images of *in vitro* fluorescence imaging of tumors from MC38 tumor-bearing mice at different time points (24 h, 48 h, 72 h, 120 h) following injection of Dil-labeled T-IBV; (J) Statistics on changes in fluorescence intensity in tumor tissue at different time points (n=3); (K) Co-localization of Dil-labeled T-IBV and TGF-β in frozen sections of tumor tissue from Dil-labeled T-IBV-treated mice at 120 h, following immunofluorescence staining (red: T-IBV; green: TGF-β; blue: cell nuclei); (L) Schematic diagram illustrating the evaluation of antitumor effects of different doses of T-IBV in MC38 tumor-bearing mice (50 μg, 100 μg, 200 μg); (M) Overall tumor growth curves in MC38 mice treated with specified doses of T-IBV (n = 7); (N) Individual tumor growth curves in MC38 mice treated with specified doses of T-IBV (n = 7). Data are shown as the mean ± standard deviation (SD). Statistical significance was determined using one-way analysis of variance (ANOVA) followed by Tukey's multiple comparisons (C, J) and a two-way ANOVA (M). *$p < 0.05$, **$p < 0.01$, ***$p < 0.001$, ****$p < 0.0001$; ns, not significant.

T-IBV Remodels the Cold Tumor Microenvironment, Triggering Local Invasion and Systemic Antitumor Immunity

The therapeutic potential of T-IBV in "cold" tumor models, characterized by weak immunogenicity, was initially assessed using a subcutaneous 4T1 breast cancer model **(Figure 4A)**. T-IBV treatment significantly inhibited subcutaneous tumor growth, as indicated by notably lower final tumor weights than in both the PBS group and the group treated with unmodified IBV **(Figure 4B-D, FigureS4, Supplementary Information)**. While IBV alone appeared to exert a modest tumor-suppressive effect, the antitumor efficacy of T-IBV was markedly greater. Immunofluorescence staining of tumor tissues further indicated increased $CD8^+$ T-cell infiltration after T-IBV treatment **(Figure 4E)**. Because *in situ* models are considered more predictive of clinical drug efficacy, we further examined the therapeutic effects of T-IBV in the more aggressive 4T1 in situ breast cancer model to assess its activity under a more clinically relevant challenge **(Figure 4F)**. In this context, T-IBV effectively inhibited primary tumor growth **(Figure 4G-J)**. Notably, T-IBV treatment substantially reduced distant tumor spread, as evidenced by an approximately 80% decrease in the number of pulmonary metastatic nodules **(Figure 4K-L)**. Histological analysis in lung tissue supported the observation that T-IBV could eliminate

pulmonary micrometastases and suppress their proliferation **(Figure 4M-N)**. This blockade of lung metastasis by T-IBV further supports its functional activity in this model.

To further elucidate the cellular immune mechanisms and antitumor effects of T-IBV, we conducted a more detailed analysis of the tumor microenvironment **(Figure 4O-S)**. Locally, T-IBV treatment was associated with a marked increase in the density of $CD8^+$ T cells infiltrating the tumor **(Figure 4O)**. At the same time, a significant reduction in Ki67 fluorescence indicated direct inhibition of tumor cell proliferation **(Figure 4P)**. Concurrently, the proportion of regulatory T cells (Tregs, $Foxp3^+$), known for their strong immunosuppressive properties, was significantly decreased at the tumor site **(Figure 4S)**. Because Tregs are a central cell subset responsible for maintaining immune tolerance in cold tumors, their reduction may indicate disrupted tumor immunosuppression [51]. With these local changes established, T-IBV treatment elicited a robust systemic antigen-specific antitumor immune response, as shown by Enzyme-linked Immunospot Assay analysis. Analysis using the Enzyme-linked Immunospot Assay (ELISPOT) confirmed that, after stimulation with the tumor-specific neoantigen peptide Zfp142 [52, 53], the number of cytotoxic T lymphocytes (CTLs) secreting IFN-γ increased markedly in the T-IBV group **(Figure 4Q-R)**. Flow cytometric analysis of splenic lymphocytes indicated that this systemic T-cell activation extended beyond the tumor site and was accompanied by increased effector memory in peripheral immune organs, including the spleen **(Figure 4T-V, Figure S5A, Supplementary Information)**. Although the proportion of myeloid suppressor cells, such as myeloid-derived suppressor cells (MDSCs), did not significantly decrease after T-IBV treatment, the overall immune response was shifted toward antitumor activity **(Figure S5B-C, Supplementary Information)**. Collectively, T-IBV effectively suppresses 4T1 cold tumors by blocking metastasis, reversing local immune tolerance, and driving $CD8^+$ T-cell activation. This local effect is accompanied by a robust systemic antigen-specific CTL response, positioning T-IBV as a promising strategy to overcome cold tumors and prevent recurrence.

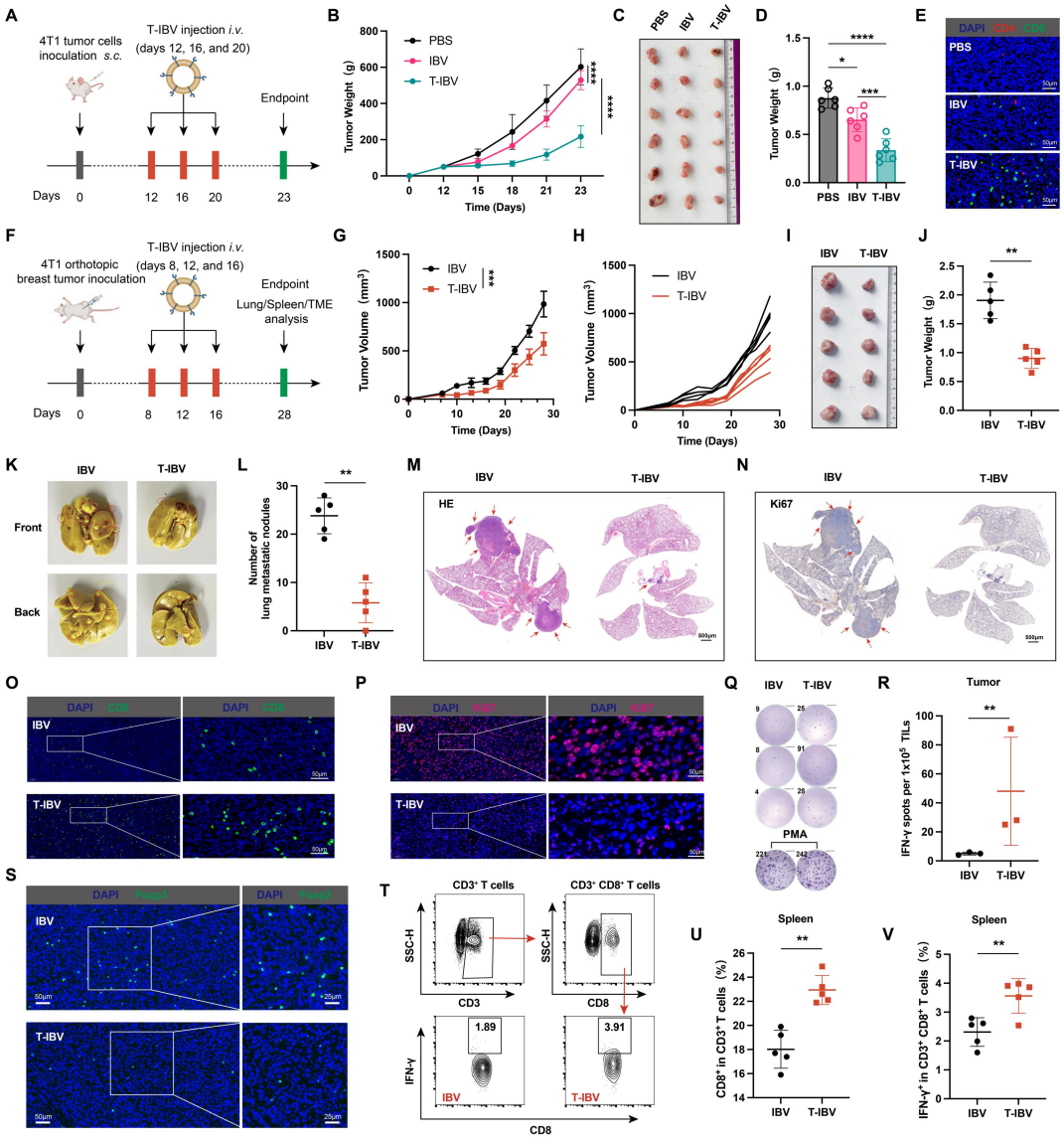

Figure 4. T-IBV promotes CTL infiltration and inhibits tumor proliferation and metastasis in cold tumors. (A) Schematic diagram illustrating the evaluation of the antitumor effects of T-IBV in a subcutaneous 4T1 model; (B) Tumor growth curves in mice after T-IBV treatment (n=6); (C) Images of 4T1 tumors in mice following dissection at the end of the experiment (Day 23); (D) Statistics on tumor weights of mice at the end of the experiment (n=6); (E) Representative immunofluorescence images of CD4 (green) and CD8 (red) in mouse tumor tissues at the end of the experiment. (F) Schematic diagram illustrating the evaluation of T-IBV's antitumor effects in a mouse orthotopic 4T1 model; (G) Overall tumor growth curves in mice after T-IBV treatment (n=5); (H) Individual tumor growth curves in mice after T-IBV treatment (n=5); (I) Images of mouse tumors after dissection on day 28 (n=5); (J) Statistics on the weight of mouse tumors excised at the end of the experiment (day 28) (n=5); (K) Representative images of pulmonary metastatic nodules in mice at the end of the experiment (day 28); (L) Statistical analysis of lung nodules in mice (n=5); (M) Representative image of lung tumor metastasis from HE-stained lung tissue analysis in mice; (N) Representative image of tumor proliferation in lung tissue from Ki67 IHC analysis in mice; (O) Representative image of CD8 (green) immunofluorescence in tumor tissue; (P) Representative image of Ki67 immunofluorescence in mouse

tumor tissue; (Q–R) Representative image (Q) and statistical analysis of spots (R, n=3) showing the number of IFN-γ-secreting T cells detected by ELISPOT 36 hours after stimulation with the 4T1 neoantigen peptide Zfp142 following lymphocyte isolation from tumor tissue; (S) Representative immunofluorescence image of the Treg marker Foxp3 in tumor tissue; (T) Representative flow cytometry and cell clustering analysis of Zfp142-specific CTLs in splenic lymphocytes following T-IBV treatment; (U) Statistical analysis of the proportion of CD8 T cells in the spleen (n=5); (V) Statistical analysis of the proportion of Zfp142-specific CTLs in the spleen (n=5). Data are shown as the mean ± standard deviation (SD). Statistical significance was determined using one-way analysis of variance (ANOVA) followed by Tukey's multiple comparisons (D) or unpaired two-tailed Student's t-tests (J, L, R, U, V), and a two-way ANOVA (B, G). *$p < 0.05$, **$p < 0.01$, ***$p < 0.001$, ****$p < 0.0001$; ns, not significant.

Integration of a uPA-Responsive PD-L1 Nanobody Blocking Module and Construction of a Bifunctional TP-IBV

We previously showed that T-IBV promotes $CD8^+$ T-cell infiltration and elevates intratumoral IFN-γ levels **(Figure 4)**. However, IFN-γ is known to drive adaptive immune resistance by inducing PD-L1 upregulation on tumor cells, which progressively dampens T-cell activity and facilitates immune escape[54, 55]. To sustain the antitumor response, a localized and precise PD-L1 blockade is required. Conventional PD-L1 monoclonal antibodies (mAbs) are limited by their large molecular weight and poor tissue penetration. Therefore, we employed a 15 kDa PD-L1 nanobody (nb), which offers superior tumor penetration and cost-effective production in *E. coli* [56, 57].

To enable spatial and temporal control of immune checkpoint blockade, we developed a uPA-responsive release module. Molecular cloning strategies enabled fusion of the high-affinity PD-L1 nb to ClyA through a substrate peptide chain ($(LSGRSDNH)_3$) recognized by urokinase-type plasminogen activator (uPA) [27], resulting in the construction of the ClyA-uPA-PD-L1 nb expression vector **(Figure 5A)**. SDS-PAGE and Western blotting confirmed the successful anchoring of PD-L1 nb to the P-IBV surface **(Figures 5B–C)**, while TEM and dynamic light scattering (DLS) demonstrated that P-IBV maintained an intact spherical structure with a uniform particle size distribution **(Figures 5D–E)**.

To validate the responsiveness of this molecular switch, we assessed PD-L1 nb cleavage and release *in vitro* and *in vivo*. *In vitro*, PD-L1 nb was cleaved and released from the vesicle surface only in the presence of recombinant uPA, as shown by the appearance of free low-molecular-weight bands on SDS-PAGE and in Western blots **(Figure 5F–H)**. *In vivo*, immunofluorescence staining of 4T1 tumor tissue confirmed significantly high expression of uPA in the tumor extracellular matrix **(Figure 5I)**, supporting intratumoral activation of P-IBV. Following intratumoral injection of P-IBV, tumor tissue homogenates were extracted, and Western blotting analysis confirmed effective cleavage of P-IBV within the tumor microenvironment **(Figure 5J–K)**. Building on the successful construction of T-IBV and P-IBV, we utilized the pRSF-Duet-1 dual-expression vector to co-express ClyA-TGFβRII and ClyA-uPA-PD-L1 nb within the same *ClearColi* system, successfully constructing the dual-engineered vesicle TP-IBV **(Figure 5L)**. Because the molecular weights of ClyA-TGFβRII (approximately 51.8 kDa) and ClyA-uPA-PD-L1 nb (approximately 51.4 kDa) are extremely close, SDS-PAGE was unable to effectively distinguish between

the two protein bands **(Figure 5M)**. However, Western blotting results using specific antibodies clearly confirmed that TP-IBV co-loaded the two functional molecules, TGFβRII and PD-L1 nb **(Figure 5N–O)**. Particle size and morphological characterization **(Figure 5P, Figure S6, Supplementary Information)** showed that co-loading the two modules did not compromise vesicle structural integrity; TP-IBV retained a uniform particle size and spherical morphology, meeting the basic physical requirements for intravenous administration. Collectively, these data demonstrate that TP-IBV successfully integrates TGF-β capture and uPA-responsive PD-L1 blockade modules while maintaining optimal physicochemical properties.

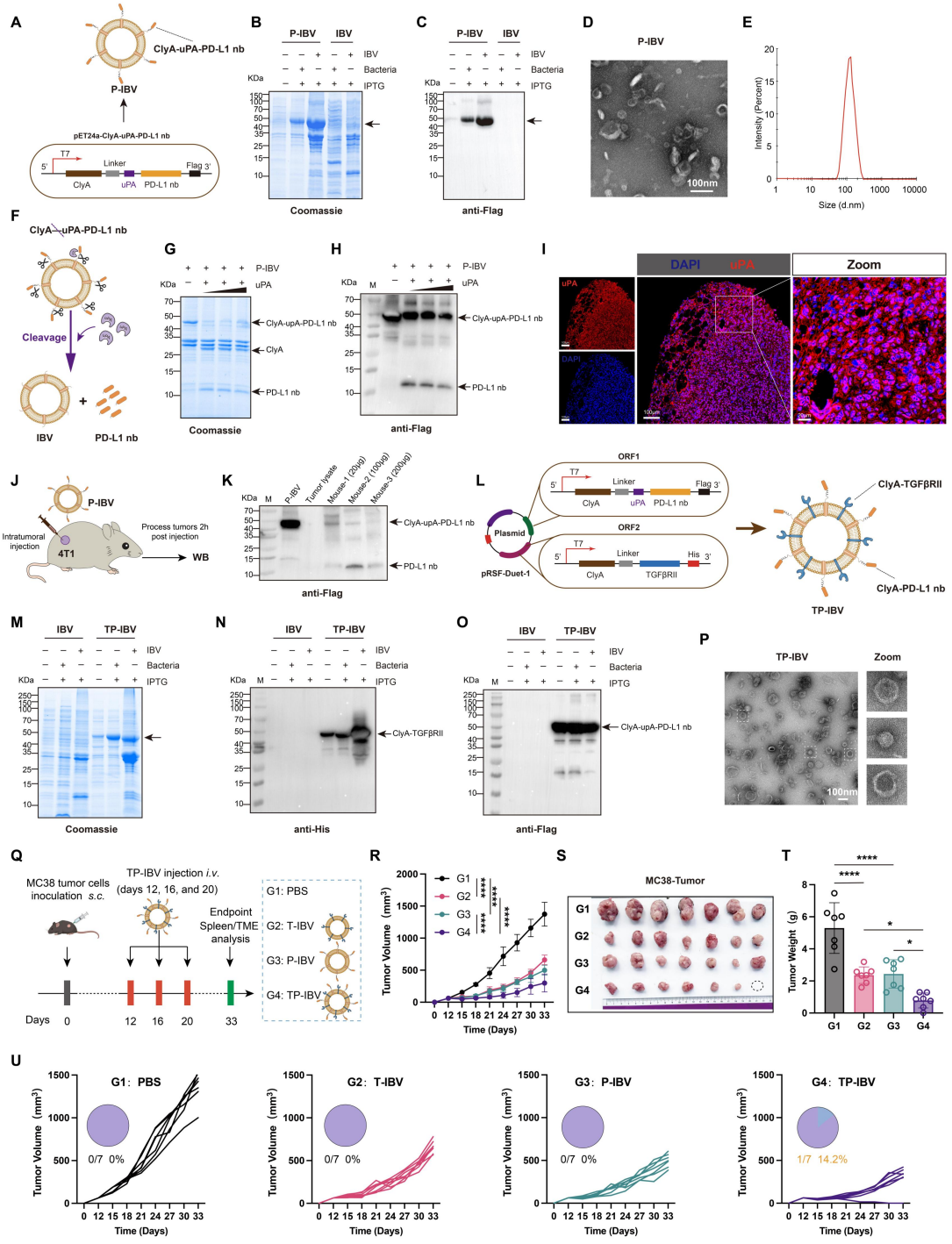

Figure 5. Construction of the bifunctional TP-IBV and evaluation of its synergistic antitumor effects. (A) Schematic diagram of the construction of the uPA-

responsive PD-L1 nb module; (B) SDS-PAGE with Coomassie staining to identify PD-L1 nb on P-IBV; (C) Western blotting analysis of PD-L1 nb expression on P-IBV using an anti-Flag antibody; (D) TEM image of purified P-IBV; (E) Particle size distribution of P-IBV measured by DLS; (F) Schematic illustration of uPA cleaving P-IBV in vitro to release the PD-L1 nb; (G) SDS-PAGE with Coomassie staining to confirm cleavage of P-IBV by uPA; (H) Western blotting using an anti-Flag antibody to analyze the release of PD-L1 nb from P-IBV following cleavage by uPA; (I) Immunofluorescence validation of uPA expression in 4T1 tumors; red: uPA; blue: cell nuclei. (J) Schematic diagram showing the detection of PD-L1 nb released by reactive cleavage from tumor tissue homogenate supernatant via Western blotting with an anti-Flag antibody 2 h after intratumoral injection of a specified dose of P-IBV; (K) Detection of PD-L1 nb release within the tumor using an anti-Flag antibody 2 h after intratumoral injection of P-IBV; (L) Schematic diagram of the construction of TP-IBV, which integrates both TGFβRII and PD-L1 nb. (M) Identification of the purified TP-IBV protein load using SDS-PAGE with Coomassie staining; (N) Validation of TGFβRII expression on TP-IBV via Western blotting using an anti-His antibody; (O) Validation of PD-L1 nb expression on TP-IBV via Western blotting using an anti-Flag antibody; (P) TEM image of purified TP-IBV; (Q) Schematic diagram of the TP-IBV treatment regimen in MC38-tumor-bearing mice; (R) Overall growth curves of mice in the designated treatment group (n=7); (S) Images of excised mouse tumors at the end of the experiment (Day 33) (n=7); (T) Statistics on the weight of excised mouse tumors (n=7); (U) Individual tumor growth curves and cure rates for mice in the designated treatment group. Data are shown as the mean ± standard deviation (SD). Statistical significance was determined using one-way analysis of variance (ANOVA) followed by Tukey's multiple comparisons (T) and a two-way ANOVA (R). *$p < 0.05$, **$p < 0.01$, ***$p < 0.001$, ****$p < 0.0001$; ns, not significant.

TP-IBV Exerts Synergistic Effects to Remodel the TME and Break Down Physical Barriers, Inducing Systemic, Long-Lasting Antitumor Immunity

After successfully developing and validating bifunctional TP-IBV *in vitro*, we evaluated whether its dual functions could produce stronger *in vivo* antitumor effects in the MC38 colorectal cancer model, as shown in **Figure 5Q**. The treatment was administered intravenously three times at three-day intervals. TP-IBV exhibited significantly greater antitumor efficacy than either monofunctional T-IBV or P-IBV. This was reflected in the tumor growth curves **(Figure 5R–T)**, and a subset of mice showed complete tumor regression, corresponding to a 14.2% cure rate. In comparison, the other treatment groups did not achieve complete tumor clearance **(Figure 5U)**. These results indicate that combining TGF-β-mediated immunosuppression blockade with enzyme-responsive PD-L1 blockade in a single vector can yield synergistic antitumor effects.

To further elucidate the cellular mechanisms underlying this synergy, we analyzed tumor-infiltrating immune cell populations by flow cytometry **(Figure S7, Supplementary Information)**. TP-IBV treatment significantly promoted polarization of tumor-associated macrophages (TAMs) toward the M1 phenotype, linked to pro-inflammatory and antitumor activity **(Figure 6A, Figure S8A, Supplementary Information)**, while notably suppressing the M2 phenotype, typically associated with

tumor progression **(Figure 6B, Figure S8B, Supplementary Information)**. This reprogramming of macrophage phenotypes is considered fundamental to reversing the immunosuppressive state of the TME. Furthermore, the proportion of natural killer (NK) cells was significantly increased in the TP-IBV group **(Figure 6C)**, strengthening innate antitumor activity. Concurrently, MDSCs, which strongly suppress immune responses in solid tumors, were substantially reduced in the TP-IBV group **(Figure 6D, Figure S9A, Supplementary Information)**. These findings suggest that TP-IBV reprograms the innate immune microenvironment to activate antitumor immunity.

At the adaptive immunity level, flow cytometry revealed that TP-IBV significantly promoted $CD8^+$ T-cell infiltration into the tumor **(Figure 6E, Figure S9B, Figure S11A, Supplementary Information)**. Notably, $CD8^+$ T-cell exhaustion was alleviated, as evidenced by the significant downregulation of the co-inhibitory receptors PD-1 and TIM-3 **(Figure 6F, Figure S9C, Supplementary Information)**. In parallel, cytotoxic T lymphocytes (CTLs) specific for the MC38 neoantigen (Adpgk) were significantly expanded within the tumor, which directly confirmed that TP-IBV induced strong antigen-specific cytotoxic activity **(Figure 6G–H)**. Immunofluorescence analysis revealed that $CD8^+$ T cells in the TP-IBV group formed dense infiltrates within the tumor parenchyma **(Figure 6I)**. In addition, terminal -deoxynucleotidyl transferase mediated nick end labeling (TUNEL) staining indicated that this robust antitumor immune response resulted in widespread apoptosis in tumor tissue **(Figure 6J)**. Collectively, these data suggest that TP-IBV alleviates T-cell exhaustion and enhances both the infiltration and cytotoxic activity of antigen-specific CTLs.

Beyond addressing immune suppression at the cellular level, we also examined TP-IBV's potential to disrupt the physical barrier of the tumor stroma. Because TGF-β is widely recognized as a key factor in promoting tumor fibrosis and activating cancer-associated fibroblasts (CAFs), we assessed this aspect using H&E staining and α-SMA immunohistochemistry. The results showed that cellular density within tumor tissue was significantly reduced in the TP-IBV group, and α-SMA expression was substantially suppressed **(Figure 6K)**. While some downregulation of α-SMA was also detected in the P-IBV group, this effect was less pronounced than in the T-IBV and TP-IBV groups, supporting the view that the anti-fibrotic effect is primarily attributable to TGF-β neutralization by T-IBV. Further, picrosirius red staining and quantitative analysis demonstrated that TP-IBV significantly reduced the deposition of dense collagen fiber networks in the tumor stroma, resulting in a sparser collagen framework **(Figure 6L–M).** Collectively, these findings suggest that TP-IBV neutralizes TGF-β, softens the physical barrier, and promotes deep infiltration of effector cells.

We further investigated whether the local therapeutic effects of TP-IBV could translate into a systemic antitumor defense. Analysis of splenic single-cell suspensions showed a significant increase in the proportion of Adpgk-antigen-specific CTLs **(Figure 6N, Figure S10, Figure S11B, Figure S12A, Supplementary Information)**, along with a corresponding decrease in splenic MDSCs **(Figure 6O, Figure S12B, Supplementary Information)**, indicating a robust systemic antitumor immune response. Notably, the proportion of central memory $CD8^+$ T cells in the spleen was significantly elevated in the TP-IBV group **(Figure 6P, Figure S12C, Supplementary Information)**. Together, the establishment of long-lived central

memory T cells is widely regarded as a key safeguard against tumor recurrence and for long-term survival, and this feature is considered to provide TP-IBV with its greatest clinical potential compared with monotherapy.

Overall, by synergistically leveraging the dual advantages of T-IBV and P-IBV, TP-IBV constructs a systemic antitumor defense mechanism: the T-IBV module neutralizes TGF-β, suppressing CAF activation and ECM collagen deposition while lifting TGF-β-mediated immune suppression in the microenvironment. Building on this, the P-IBV module responds to highly expressed uPA in the tumor microenvironment by releasing small-sized PD-L1 nanobodies locally at the tumor site, blocking the PD-1/PD-L1 signaling axis and reversing the exhaustion of $CD8^+$ T cells (Figure 6Q). This cascading strategy not only efficiently reshapes the immune landscape of local tumors but also induces systemic, antigen-specific, and durable antitumor immunity.

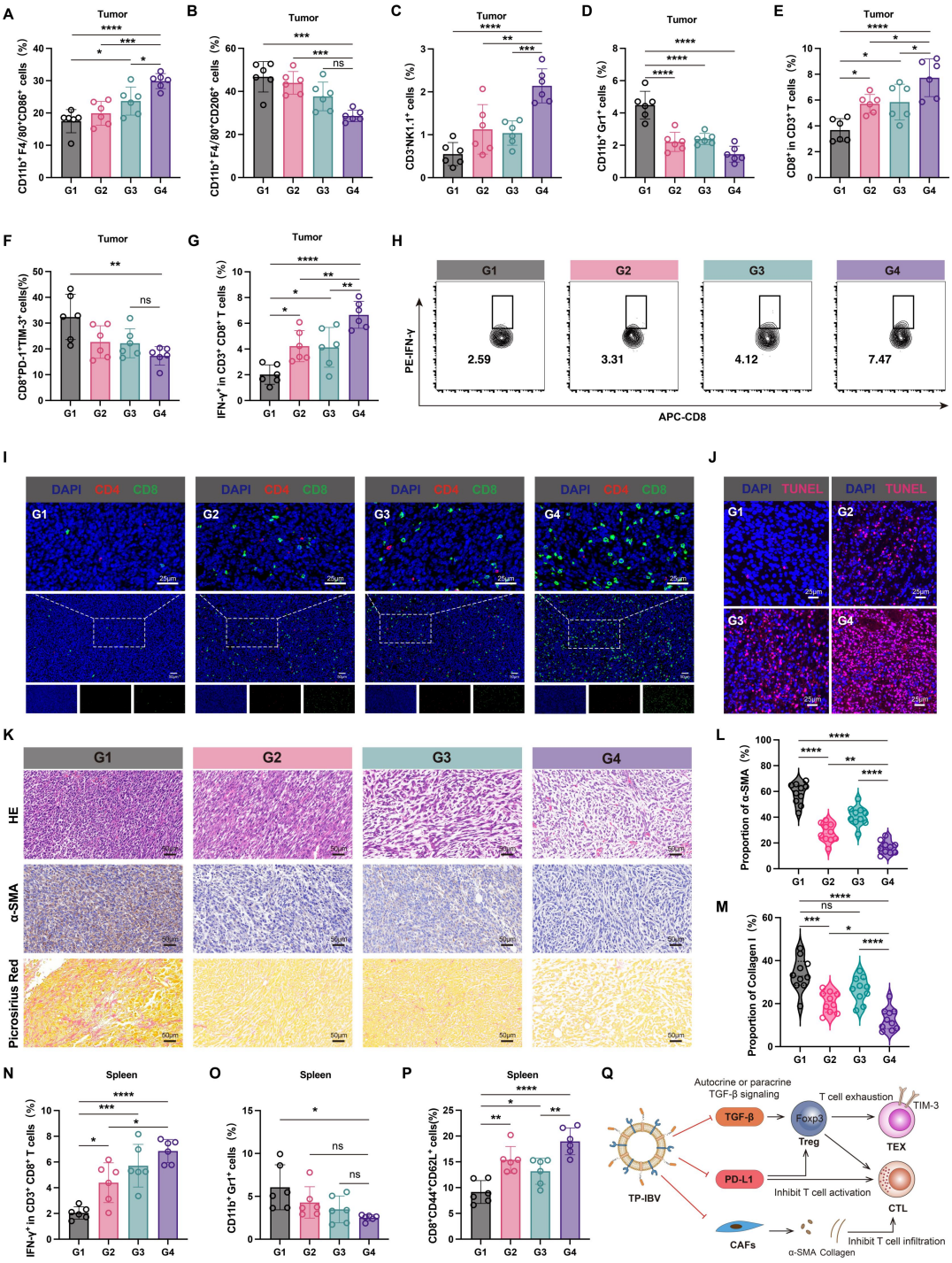

Figure 6. TP-IBV reduces tumor α-SMA and collagen expression and induces a significant antitumor immune phenotype. (A) Flow cytometry analysis of the proportion of M1 TAMs ($CD11b^+F4/80^+CD86^+$) in the TME (n=6); (B) Flow cytometry analysis of the proportion of M2 TAMs ($CD11b^+F4/80^+CD206^+$) in the TME (n = 6); (C) Flow cytometry analysis of the proportion of NK cells ($CD3^-NK1.1^+$) in the TME (n = 6); (D) Flow cytometric analysis of the proportion of MDSCs ($CD11b^+Gr\text{-}1+$) in the TME (n=6); (E) Flow cytometric analysis of the proportion of CD8 T cells ($CD3^+CD8^+$) in the TME (n=6); (F) Flow cytometric analysis of the proportion of exhausted T cells ($CD8^+PD\text{-}1^+TIM\text{-}3^+$) in the TME (n=6); (G–H) Flow cytometric analysis of the proportion of CTL cells ($CD3^+CD8^+IFN\text{-}\gamma^+$)

specific for the tumor neoantigen Adpgk in the TME (G) and representative flow cytometry figure (H) (n=6); (I) Representative immunofluorescence images of CD4 and CD8 T cells in tumor tissues from different treatment groups (blue: cell nuclei; red: CD4 T cells; green: CD8 T cells) ; (J) Representative TUNEL images of tumor tissues from different treatment groups; (K) Representative images of formalin-fixed, paraffin-embedded tumor sections from different treatment groups showing hematoxylin-eosin (H&E) staining for collagen (top), anti-α-SMA IHC staining (middle), or Sirius Red staining (bottom); (L–M) For quantitative analysis, the number of α-SMA+ pixels (L) or collagen+ pixels (M) was measured in multiple regions of interest (ROIs) for each tumor and normalized to the corresponding ROI area (n = 10); (N) Flow cytometry analysis of the proportion of Adpgk neoantigen-specific CTLs ($CD3^+CD8^+IFN\text{-}\gamma^+$) in the spleen (n=6); (O) Flow cytometry analysis of the proportion of MDSCs ($CD11b^+Gr\text{-}1^+$) in the spleen (n=6); (P) Flow cytometry analysis of the proportion of CD8 central memory T cells ($CD8^+CD44^+CD62L^+$) in the spleen (n=6); (Q) Schematic diagram illustrating the mechanism by which TP-IBV exerts a synergistic antitumor effect. TP-IBV exerts a synergistic antitumor effect by neutralizing autocrine/paracrine TGF-β in the TME, thereby inhibiting Treg and exhausted T cell formation, while reducing TGF-β-induced ECM formation and blocking the PD-L1 inhibitory pathway, which promotes CD8 T cell infiltration. Data are shown as the mean ± standard deviation (SD). Statistical significance was determined using one-way analysis of variance (ANOVA) followed by Tukey's multiple comparisons (A–G, L–P). *$p < 0.05$, **$p < 0.01$, ***$p < 0.001$, ****$p < 0.0001$; ns, not significant.

Multidimensional Transcriptomic Analysis of TP-IBV-Mediated Remodeling of the Cold Tumor Microenvironment

In the 4T1 cold tumor model, we compared TP-IBV with a combination strategy that more closely reflects clinical practice. This strategy consisted of T-IBV administered alongside an anti-PD-L1 monoclonal antibody. In this approach, we administered 200 μg of PD-L1 mAb intravenously to each mouse two days after T-IBV injection **(Figure 7A)**. The findings indicated that PD-L1 mAb alone produced tumor suppression comparable to T-IBV, while the combination of T-IBV and PD-L1 mAb was more effective than either treatment alone. Notably, TP-IBV exhibited significantly greater efficacy than the T-IBV and PD-L1 mAb combination therapy **(Figure 7B–D, Figure S13, Supplementary Information)**. This result highlights the rationale for the study, which is that the integrated nanocarrier design may better coordinate both functional modules at the same tumor site. The responsive release mechanism and the small size of the nanobodies are likely to contribute to enhanced penetration into deeper tumor tissue. Achieving such precise spatiotemporal synergy is challenging when using two independent macromolecular antibody systems.

To thoroughly analyze the mechanisms underlying treatment-induced immune remodeling of the TME, we isolated tumor RNA on day 27 after TP-IBV treatment and performed transcriptomic sequencing. Principal component analysis (PCA) showed that the five experimental groups formed spatially distinct, clear clusters **(Figure S14A, Supplementary Information)**. In contrast, Venn diagram analysis further revealed that each treatment group (G1–G5) possessed its own unique set of

differentially expressed genes, indicating that each treatment modality was highly distinctive and comprehensive **(Figure S14B, Supplementary Information)**. Heatmap analysis of overall immune gene modules **(Figure 7E-H)** showed that, compared with groups treated with T-IBV alone, ICB alone, or both drugs, the TP-IBV treatment group (G5) exhibited global, multidimensional immune activation. This was manifested by significantly higher expression of immune stimulation-related genes such as Lck, Lat, and Stat1; upregulation of antigen presentation-related genes such as H2-M5, CD74, and Tap1; and a coordinated increase in adaptive immune system genes such as CD3e, CD36, and CD28, alongside chemokine/receptor genes such as Ccl5 and Cxcl10. Furthermore, TP-IBV significantly upregulated innate immune genes including Nos2, Cxcl3, and Ccl7 **(Figure S14C, Supplementary Information)**. Interestingly, inhibitory receptors such as Cd274, Cd200r1, and Pdcd1 also exhibited a significant upregulation trend in the TP-IBV group **(Figure S14E, Supplementary Information)**.

The immune cell subset profile **(Figure 7I)** further supported TP-IBV's therapeutic effects at the cellular level. Marker genes for various effector immune cells were significantly upregulated, including cytotoxic T cells (Cd8a, Gzmb, Prf1), helper T cells (Th1, Th2), NK cells, and activated dendritic cells. Moreover, the signature genes of iNOS+ tumor-associated macrophages (TAMs) were markedly upregulated in the TP-IBV group **(Figure S14D, Supplementary Information)**. Transcriptomic enrichment analysis showed that TP-IBV-upregulated genes were primarily enriched in the JAK-STAT pathway, antigen processing and presentation, NK cell-mediated cytotoxicity, and cytokine-receptor interactions **(Figure S15A-B, Supplementary Information)**.

To further investigate how TP-IBV affects the TGF-β signaling pathway and ECM remodeling, we examined key molecules upstream and downstream of the pathway **(Figure 7K–N)**. Tgfbr2, Smad2, and the classical downstream pro-fibrotic target genes Ctgf (Ccn2) and Serpine1 (PAI-1) were significantly downregulated in the TP-IBV group. Consistent with this pathway inhibition, matrix remodeling-associated genes, including the CAF activation marker Fap, various collagens (Col3a1, Col4a1, Col5a1), fibronectin 1 (Fn1), and matrix metalloproteinases MMP2 and MMP14, were all significantly suppressed **(Figure S16A–G, Supplementary Information)**. Pathway enrichment analysis revealed that these downregulated genes were highly concentrated in ECM receptor interactions, cell adhesion molecules, ECM organization, and collagen chain trimerization **(Figure S15C–E, Supplementary Information)**. In addition to removing this physical barrier, TP-IBV treatment significantly activated key signaling pathways associated with innate immunity and tumor stress **(Figure S16H–L, Supplementary Information)**. The expression levels of the interferon-induced GTPase Gbp5 and the dendritic cell activation transcription factor Batf2 were substantially elevated, confirming highly active interferon signaling in the tumor microenvironment. At the same time, Raet1e, a key activation ligand for NK cells and T cells, was significantly upregulated, indicating that tumor cells were under considerable immune pressure and were actively releasing attack signals. Furthermore, we observed elevated expression of the myeloid mobilization factor Csf3 and the cytokine Il24, which directly promotes tumor cell apoptosis, further amplifying immune inflammation and direct cytotoxic effects.

It is noteworthy that, with respect to cytotoxic molecules and specific CTL effects, the heatmap in **Figure 7O** visually demonstrates that the gene expression levels of several core cytotoxic molecules, including Ifng, Nkg7, Gzmb, and Prf1, were

markedly upregulated in the TP-IBV group, far exceeding those observed in the T-IBV plus PD-L1 mAb combination group, where only a few genes showed mild upregulation. To further validate the cytotoxic activity of functional T cells, we isolated tumor-infiltrating lymphocytes and stimulated them with the neoantigen peptide Zfp142 (Figure 7P–Q). Quantitative ELISPOT results confirmed that TP-IBV induced a significant increase in the number of cells forming IFN-γ secretion spots, and that the antigen-specific CTL response it induced was much higher than in the T-IBV monotherapy and combination therapy groups. In line with these findings, tumor immunofluorescence confirmed extensive infiltration of CD8 T cells and substantial granzyme B release (Figure 7R). Collectively, these transcriptomic and functional analyses demonstrate that TP-IBV simultaneously dismantles the stromal barrier and triggers robust innate and adaptive immune activation. This integrated delivery platform ultimately drives a superior antigen-specific cytotoxic T cell response compared with conventional combination antibody therapy.

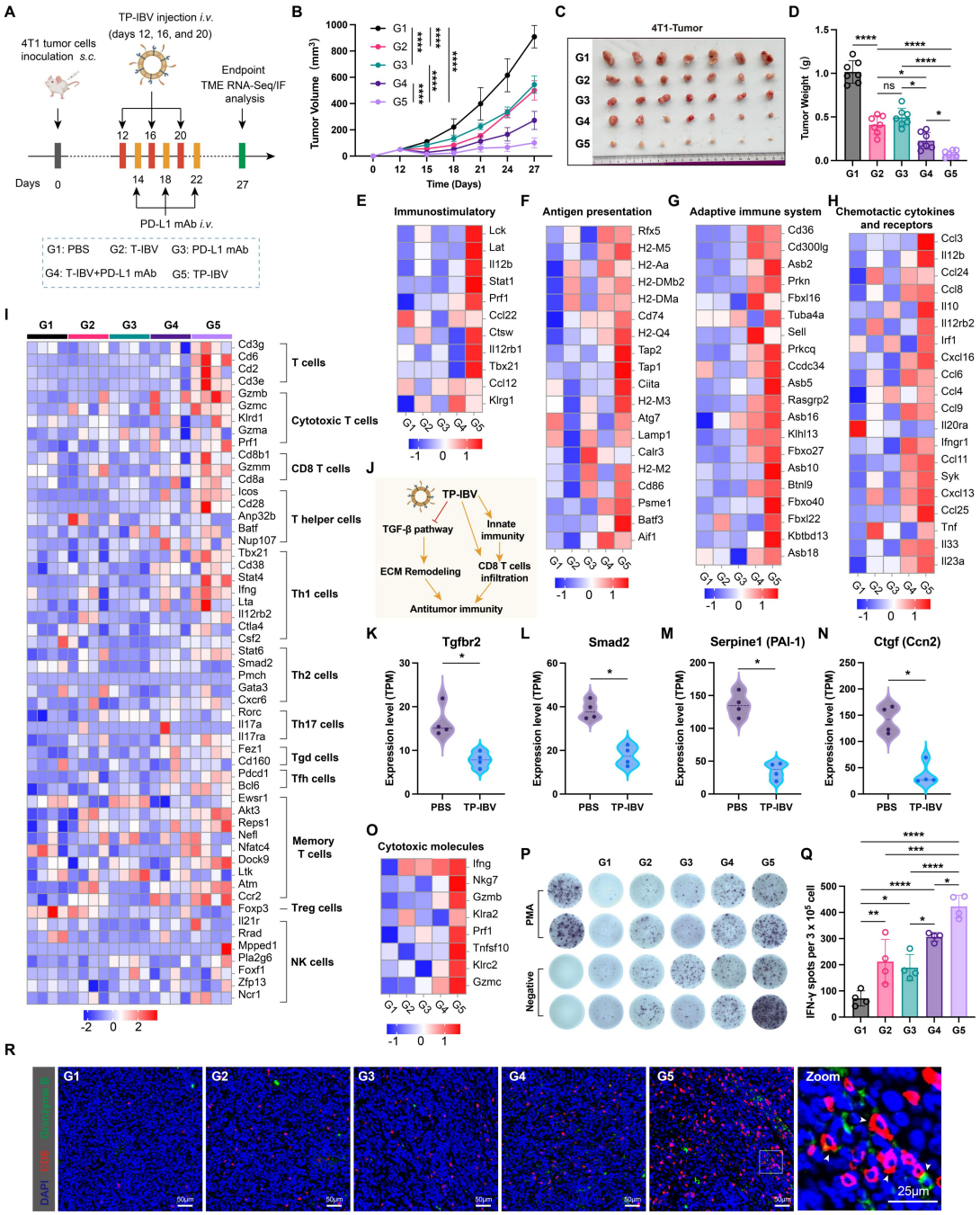

Figure 7. Multidimensional analysis of the mechanisms by which TP-IBV induces cold tumor remodeling of the TME. (A) Schematic diagram of the evaluation process for different treatment groups in the 4T1 model; (B) Overall tumor growth curves for different treatment groups (n=7); (C) Histological images of tumors from different treatment groups at the end of the experiment (n=7); (D) Statistics on the weight of resected tumors (n=7); (E – H) Heatmaps of RNA-seq data showing gene expression related to immune regulation (E), antigen presentation (F), the adaptive immune system (G), and chemokines and receptors (H) in tumor tissues from mice treated with PBS, T-IBV, PD-L1 mAb, T-IBV + PD-L1 mAb, and TP-IBV. Data for each gene are visualized as z-scores of gene expression levels normalized to the PBS-treated group (n = 4; mean values shown). Heatmaps of immune stimulatory factor gene expression across different experimental groups: (I) Heatmap showing

gene expression associated with different immune cell types in tumor tissues from mice in each designated treatment group. Data for each gene are presented as z-scores of gene expression levels normalized to the PBS group (n = 4); (J) A schematic diagram summarizing the mechanism by which TP-IBV activates antitumor activity; (K – N) Gene expression levels upstream and downstream of the TGF β signaling pathway following TP-IBV treatment, including Tgfbr2 (K), Smad2 (L), Serpine1 (M), and Ctgf (N); (O) Heatmap of cytotoxic molecule expression across different treatment groups (n = 4). (P – Q) ELISPOT images (P) and statistical analysis of spots (Q) 36 h after stimulation of tumor immune cells with the tumor neoantigen peptide Zfp142 (n = 4). (R) Representative immunofluorescence images of CD8 (red) and granzyme B (green) in tumor tissues from different treatment groups. Data are shown as the mean ± standard deviation (SD). Statistical significance was determined using one-way analysis of variance (ANOVA) followed by Tukey's multiple comparisons (D, Q) or unpaired two-tailed Student's t-tests (K – N), and a two-way ANOVA (B). *$p < 0.05$, **$p < 0.01$, ***$p < 0.001$, ****$p < 0.0001$; ns, not significant.

TP-IBV induces GSDMD/GSDME dual-pathway pyroptosis to trigger DAMP release and amplify central trained immunity

In addition to the previously discussed multidimensional mechanisms involved in TME remodeling, TP-IBV robustly activates immunogenic cell death pathways in tumor cells. Transcriptomic sequencing revealed that GSDMD expression was markedly upregulated in the T-IBV, T-IBV+PD-L1 mAb, and TP-IBV groups, with the largest increase in the TP-IBV group. In contrast, PBS and PD-L1 mAb alone did not induce significant expression **(Figure 8A)**. Concurrently, GSDME showed very low baseline expression in 4T1 tumors but was highly expressed specifically in the T-IBV+PD-L1 mAb and TP-IBV treatment groups **(Figure 8A)**. The parallel expression patterns of GSDME and GzmB **(Figure 7O)** suggested an association. Immunofluorescence further confirmed a significant increase in GSDMD fluorescence intensity in TP-IBV-treated tumor tissues, along with clear colocalization of GSDME and GzmB within the tumor region **(Figure 8B)**. Consistent with the transcriptomic profiling that revealed profound enrichment of $iNOS^+$ TAM signature genes **(Figure 7I and Figure S14D, Supplementary Information)**, immunofluorescence further confirmed a massive infiltration of $iNOS^+$ TAMs with antitumor activity in the TP-IBV-treated microenvironment **(Figure 8C)**.

To clarify the specific effects of cell death in vitro, we co-incubated T-IBV, P-IBV, and TP-IBV with 4T1 cells. All three vesicle treatments effectively induced tumor cell death, as shown by a significant increase in SYTOX green fluorescence. This effect was significantly reversed by the pyroptosis inhibitor Necrosulfonamide (NSA) **(Figure 8D–E)**. At the molecular level, T-IBV, P-IBV, and TP-IBV did not directly cleave GSDME, and consequently, no N-terminal functional domain of GSDME was generated **(Figure 8F)**. However, NSA treatment significantly inhibited the increased release of LDH and ATP observed in the cell culture supernatant **(Figure 8G–H)**. These findings indicate that TP-IBV can directly induce classic immunogenic cell death (ICD) in tumor cells. A hallmark of ICD is the massive release of DAMPs, such as HMGB1. HMGB1 can activate downstream signaling pathways via receptors such as RAGE and TLR2/4 [58]. More importantly, HMGB1 potently induces trained immunity **(Figure 8I)**. Using an *in vitro* BMDM training model, we demonstrated that HMGB1 pretreatment significantly enhanced the ability of macrophages to secrete IL-6 upon secondary stimulation **(Figure 8J)**.

To determine the relative contributions of pyroptosis and effector cells to the overall antitumor process, and to validate the source of GSDME cleavage *in vivo*, we performed pharmacological interventions and antibody depletion experiments **(Figure 8K)**. We verified the efficiency of CD8 T cell and NK cell depletion using anti-CD8 mAb and anti-AS-GM1, respectively **(Figure S17, Supplementary Information)**. Following GSDMD inhibition with disulfiram, the tumor growth curve rebounded, and tumor weight and volume were significantly greater than in the TP-IBV group, although still lower than in the PBS group **(Figure 8L–N)**. Similarly, depleting CD8 T cells or NK cells, either individually or in combination, produced a comparable trend of accelerated tumor growth. Western blot results showed that disulfiram treatment, $CD8^+$ T cell depletion, or NK cell depletion significantly reduced GSDME cleavage in tumor tissue **(Figure 8O)**. These findings confirm that GSDMD-mediated pyroptosis and GSDME cleavage, which is mediated by GzmB from CD8 and NK cells, represent two parallel and indispensable mechanisms through which TP-IBV exerts its antitumor effects.

It has been confirmed in **Figure 2** that IBV alone can directly establish central trained immunity in the bone marrow. We further examined the role of TP-IBV-induced pyroptosis in this process by isolating bone marrow at the end of the experiment (Day 27), differentiating the cells into BMDMs, and subjecting them to secondary stimulation with LPS, Pam3CSK4, and 4T1 tumor lysate **(Figure 8P)**. When pyroptosis was inhibited using disulfiram, the ability of BMDMs to secrete IL-6 and TNF-α upon secondary stimulation remained higher than that of the PBS group but was significantly weaker than that of the unblocked TP-IBV group **(Figure 8Q–R)**. This demonstrates that while IBV alone can induce baseline trained immunity, the pyroptosis and subsequent DAMP release triggered by TP-IBV are required to amplify this central trained immunity.

Collectively, these results demonstrate that TP-IBV induces ICD and dual-pathway pyroptosis in tumor cells, characterized by GSDMD activation and GzmB-dependent GSDME cleavage. The resulting release of DAMPs, particularly HMGB1, amplifies the baseline central trained immunity established by the IBV chassis, ultimately contributing to the sustained antitumor efficacy.

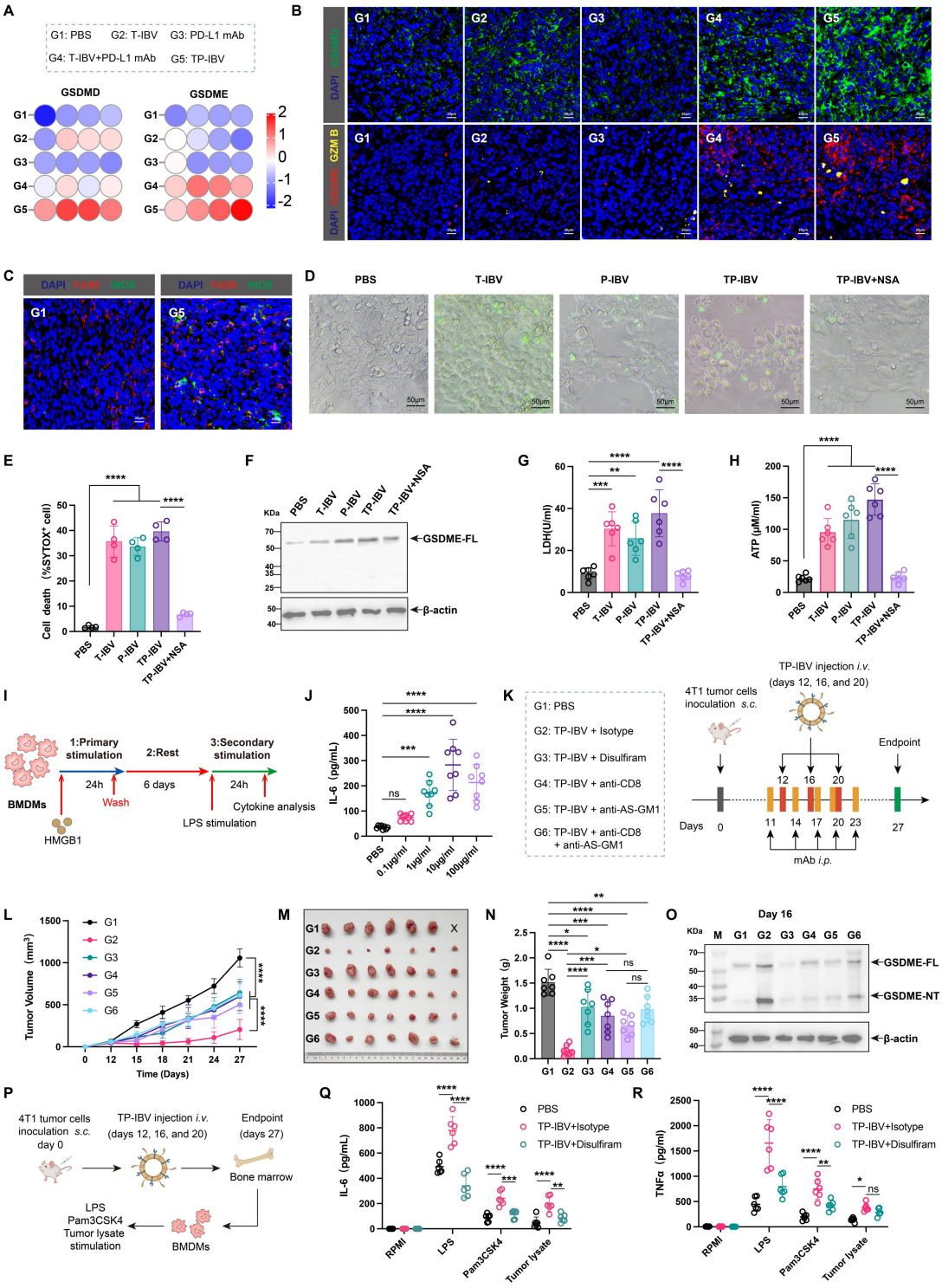

Figure 8. TP-IBV induces tumor regression through GSDMD/GSDME dual-pathway pyroptosis and amplifies central trained immunity. (A) RNA-seq heatmap showing GSDMD and GSDME gene expression levels in tumor tissues after treatment in different groups (n=4); (B) Distribution of GSDMD, GSDME, and granzyme B in tumor tissues from different designated treatment groups (green: GSDMD; red: GSDME; yellow: granzyme B; blue: DAPI). (C) Fluorescent distribution of iNOS-expressing tumor-associated macrophages in tumors from the TP-IBV treatment group (red: F4/80; blue: cell nuclei; green: iNOS). (D) Cell images

of 4T1 cells co-incubated with different engineered IBV variants for 24 h; green indicates dead cells. GSDMD inhibitor: Necrosulfonamide (NSA); green fluorescent probe: SYTOX Green; (E) Statistical analysis of SYTOX Green^{+} cell death rates (n=4); (F) Western blot analysis of GSDME cleavage, a pyroptosis-related protein, in different treatment groups after 24-hour co-incubation with 4T1 cells, with β-actin as the loading control; (G-H) Detection of LDH (G) and ATP (H) release levels in 4T1 cell culture supernatants after treatment with different groups (n=6). (I) Schematic diagram illustrating the process of inducing immunological training in BMDMs with different concentrations of HMGB1. (J) IL-6 secretion levels in BMDMs following LPS re-stimulation 6 days after stimulation with different concentrations of HMGB1 (n=8); (K) Schematic diagram of the intervention on 4T1 tumors following GSDMD inhibitor suppression and in vivo clearance by NK and CD8 T cells; (L) Overall tumor growth curves after intervention in different designated treatment groups (n=7); (M) At the end of the experiment, images of tumors isolated from different groups; black crosses indicate mouse death (n=7); (N) Statistical analysis of tumor weight data across different experimental groups (n=7). (O) Western blotting analysis of GSDME cleavage in tumor tissue homogenates after intervention in different designated treatment groups on day 16. (P) Schematic diagram of the central training-induced immune process at the end of the experiment: bone marrow cells were isolated and differentiated in vitro into BMDMs; cytokine levels were then measured after 24 hours of re-stimulation with different stimulants to evaluate the process. (Q–R) ELISA detection of IL-6 and TNF-α cytokine levels in BMDMs stimulated with different stimuli (n=6). Data are shown as the mean ± standard deviation (SD). Statistical significance was determined using one-way analysis of variance (ANOVA) followed by Tukey's multiple comparisons (D, F, G, I, N) or a two-way ANOVA (Q, R). *$p < 0.05$, **$p < 0.01$, ***$p < 0.001$, ****$p < 0.0001$; ns, not significant.

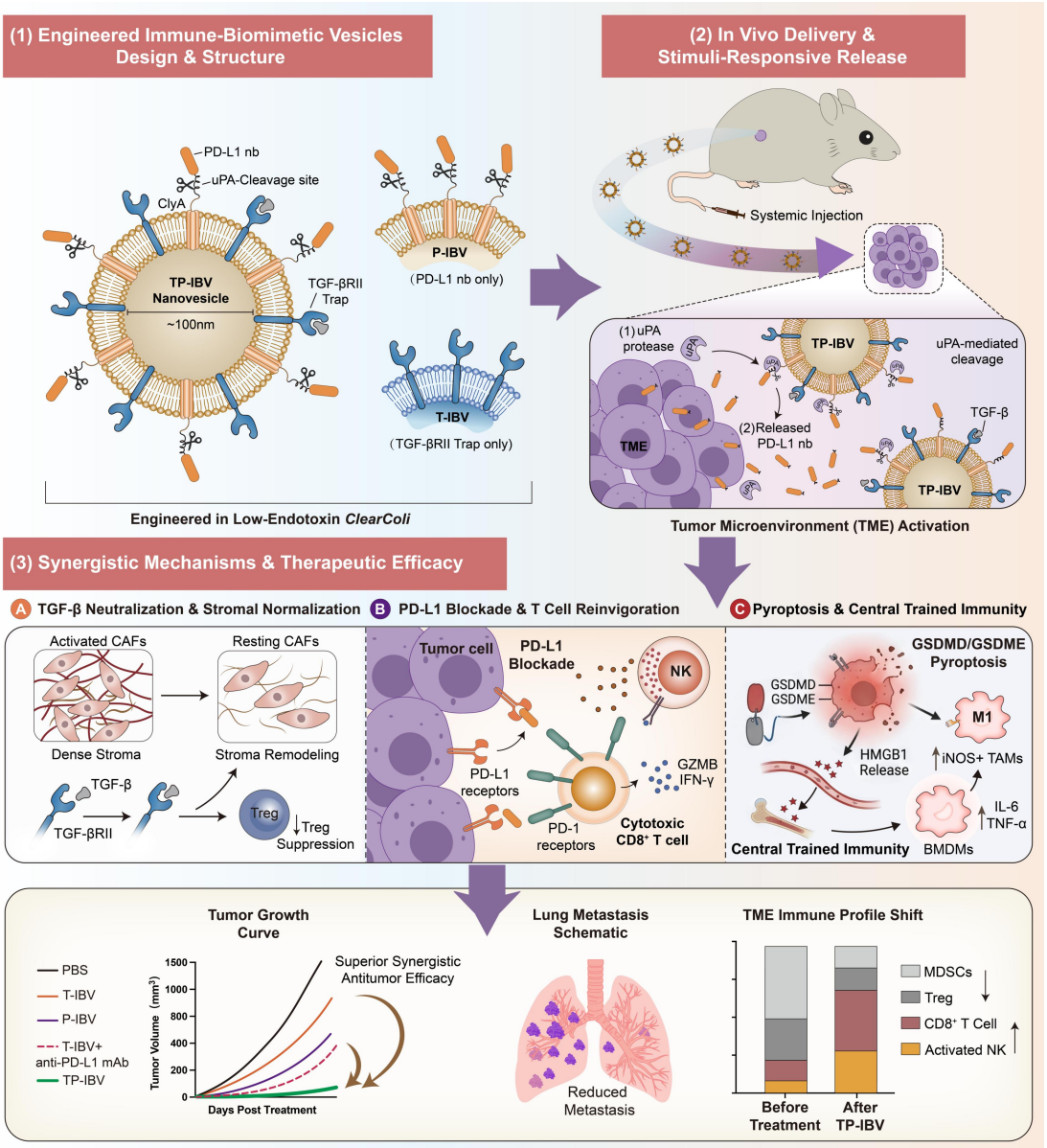

Figure 9. Schematic illustration of the rational design, in vivo delivery, and synergistic antitumor mechanisms of TP-IBV.

(1) Design and structural features. TP-IBV is engineered using a low-endotoxin *ClearColi* chassis. The vesicle surface (approximately 100 nm) co-displays two functional modules: a TGF-βRII extracellular domain acting as a decoy receptor (T-IBV module) and a PD-L1 nanobody (PD-L1 nb) conjugated via a uPA-cleavable peptide linker (P-IBV module). **(2) *In vivo* delivery and stimuli-responsive release.** Following systemic administration, TP-IBV accumulates in the tumor microenvironment (TME). Elevated uPA protease activity in the TME specifically cleaves the linker, enabling the localized release of the PD-L1 nb. Concurrently, the surface-anchored TGF-βRII traps and neutralizes TGF-β. **(3) Synergistic mechanisms and therapeutic efficacy.** The integrated design triggers a triad of antitumor effects: (A) TGF-β neutralization and stromal normalization. TGF-β trapping reverses cancer-associated fibroblast (CAF) activation, remodels the dense extracellular matrix (ECM) stroma, and suppresses regulatory T cell (Treg) activity;

(B) PD-L1 blockade and T-cell reinvigoration. The locally released PD-L1 nb blocks the PD-1/PD-L1 axis, alleviating T-cell exhaustion and reinvigorating cytotoxic $CD8^+$ T cells and natural killer (NK) cells to secrete granzyme B (GzmB) and IFN-γ; (C) Dual-pathway pyroptosis and central trained immunity amplification. Together, these effects drive GSDMD- and GSDME-dependent tumor cell pyroptosis, resulting in massive release of DAMPs, particularly HMGB1. Locally, HMGB1 repolarizes tumor-associated macrophages (TAMs) toward a pro-inflammatory M1-like phenotype, increasing $iNOS^+$ TAMs and IL-6/TNF-α secretion. Systemically, this HMGB1 feedback acts as an adjuvant, amplifying baseline central trained immunity in bone marrow-derived macrophages (BMDMs). Ultimately, TP-IBV achieves superior synergistic antitumor efficacy, significantly inhibiting primary tumor growth and reducing lung metastasis compared to monotherapies or conventional antibody combinations. This is accompanied by a robust shift in the TME immune profile, characterized by decreased MDSCs and Tregs alongside significantly increased $CD8^+$ T cells and activated NK cells.

Conclusions and Discussion

This study aimed to address the clinical challenge posed by the combined inhibitory effects of TGF-β and PD-L1 in solid-tumor immunotherapy. To overcome this, we developed and validated a dual-function immunomodulatory platform, TP-IBV, using engineered attenuated bacterial vesicles. By integrating a TGF-βRII decoy receptor and a uPA-responsive PD-L1 nanobody onto a low-endotoxin *ClearColi* chassis, TP-IBV achieves spatiotemporally coordinated immunomodulation. Our data demonstrate that this integrated nanocarrier design fundamentally outperforms conventional combination therapies in the 4T1 cold tumor model **(Figure 7B-D).**

The *ClearColi* platform achieves a critical balance between safety and innate immunogenicity. A major bottleneck for bacterial vesicle-based therapies is the risk of cytokine storms driven by wild-type endotoxin. The *ClearColi* strain significantly reduces this endotoxin load while retaining a mild adjuvant effect. Our acute-phase cytokine kinetics revealed a distinct transient pattern that returned to baseline within 12 hours **(Figure 3D-G)**, indicating a self-limiting, acute immunostimulation rather than persistent chronic inflammation. Anatomical mapping of this innate memory confirmed that a single intravenous injection establishes persistent trained immunity lasting at least 30 days, initiated in the bone marrow and extending to the spleen and lymph nodes, while sparing the lungs **(Figure 2I-Q)**. This pre-established trained state provides a robust biological foundation for subsequent adaptive immune activation.

The T-IBV module uses TGFβRII to neutralize TGF-β1/2/3 broadly. Prior studies have established that TGF-β acts as a primary driver of immune evasion by promoting T-cell exclusion within the TME, a mechanism that significantly attenuates the efficacy of PD-L1 blockade [9, 15, 59]. While conventional neutralizing antibodies or small-molecule inhibitors struggle with rapid clearance and insufficient localized targeting[59], our nanovesicle platform overcomes these limitations through design.

Leveraging the multivalent and high-density display of TGFβRII on the vesicle surface, this decoy strategy enables active anchoring to TGF-β within the tumor microenvironment. This interaction ensures long-term nanocarrier retention and significantly reduces nonspecific uptake by the reticuloendothelial system **(Figure 3I-K)**. By inhibiting CAF activation and collagen deposition **(Figure 6K-M),** T-IBV physically dismantles the fibrotic barrier and achieves an ~80% inhibition rate of lung metastasis in the 4T1 model **(Figure 4K-L)**, validating its efficacy against TGF-β-driven epithelial-mesenchymal transition [60]. However, T-IBV monotherapy plateaued at ~100 μg. It is well established that IFN-γ signaling, while essential for cytotoxic T cell function, can drive the expression of checkpoint molecules such as PD-L1 on tumor cells, a process that constitutes a classic hallmark of adaptive immune resistance[54, 61]. Mechanistically, this induction is primarily mediated through the IFNGR–JAK–STAT1–IRF1 signaling axis[62]. Chronic or persistent IFN-γ exposure can further establish a feedback loop that progressively blunts immune activation. In our transcriptomic profiling, we observed that the pronounced immune activation in the TP-IBV group was accompanied by a compensatory upregulation of multiple inhibitory receptors, including *Cd274* (encoding PD-L1), *Pdcd1*, and *Cd200r1* **(Figure S14E, Supplementary Information)**. This observation aligns with the established paradigm that a robust antitumor immune response triggers feedback-mediated inhibitory signaling within the tumor microenvironment. This mechanistic bottleneck, where initial immune activation is progressively dampened by adaptive resistance, provided the fundamental rationale for integrating a PD-L1 blockade module to sustain the antitumor response. To overcome the poor tissue penetration of conventional mAbs, we utilized a 15 kDa PD-L1 nanobody released via a uPA-cleavable linker. This dual-control release strategy ensures that the physical barrier is addressed before the immune inhibition is disrupted.

The integrated design achieves spatiotemporal synergy and broad transcriptomic reprogramming. When TGF-β neutralization and PD-L1 blockade are applied to the same spatial scale on a single vesicle, a superadditive synergistic improvement is observed. Transcriptomic profiling of the TME revealed a global, multidimensional immune activation driven by TP-IBV **(Figure 7E-H)**. Key signaling pathways, including JAK-STAT, antigen processing, and NK cell-mediated cytotoxicity, were globally elevated **(Figure S15A-B, Supplementary Information)**. Transcriptomic profiling revealed pronounced enrichment of $iNOS^+$ TAM signature genes **(Figure 7I and Figure S14D, Supplementary Information)**, a phenotypic shift further validated at the protein and cellular levels by the massive infiltration of $iNOS^+$ TAMs observed in tumor tissue immunofluorescence **(Figure 8C)**. Concurrently, the coordinated downregulation of ECM receptor interactions and collagen assembly pathways **(Figure S15C-E, Supplementary Information)** precisely elucidates how TP-IBV disrupts the physical barrier while reshaping innate immune phenotypes. Interestingly, this robust immune activation state was also accompanied by the upregulation of a broader panel of inhibitory receptors, including *Cd274*, *Cd200r1*, and *Pdcd1* **(Figure S14E, Supplementary Information)**. This compensatory response reflects the dynamic balance between effector functions and regulatory

feedback within the TME, further confirming the intense immune activation driven by TP-IBV.

TP-IBV triggers a dual-pathway pyroptosis cascade, shifting the TME from passive relief to active provocation. Beyond merely neutralizing suppressive signals, TP-IBV actively executes a highly immunogenic form of cell death. While TGF-β trapping and PD-L1 blockade primarily release the brakes on existing effector cells, pyroptosis actively provokes the immune system by converting dying tumor cells into an *in situ* vaccine. *In vitro*, the vesicles directly induced tumor cell death in an NSA-sensitive manner, accompanied by significantly increased LDH and ATP release **(Figure 8D-E, 8G-H)**, confirming classic ICD induction. *In vivo*, the functional contribution of GSDMD-dependent pyroptosis was validated by pharmacological inhibition; blocking GSDMD with disulfiram significantly attenuated the antitumor efficacy of TP-IBV compared to the unblocked group **(Figure 8L-N)**. In contrast, GSDME cleavage and activation depended strictly on granzyme B released by $CD8^+$ T cells and NK cells, as evidenced by the *in vivo* depletion experiments **(Figure 8O)**. This sequential collaborative model, which involves GSDMD-mediated initiation followed by granzyme B/GSDME-mediated amplification, constitutes the core mechanism of TP-IBV-induced highly immunogenic cell death, ultimately driving the massive release of DAMPs.

The HMGB1-mediated feedback loop amplifies central trained immunity. Beyond remodeling the local TME, DAMPs released from *in situ* tumor pyroptosis serve as a systemic signal that feeds back to the bone marrow. Our *in vitro* BMDM experiments provided rigorously controlled evidence for this cascade. Specifically, when GSDMD pyroptosis was blocked with disulfiram, the baseline trained immunity induced by the IBV chassis was preserved but significantly weaker than in the unblocked TP-IBV group **(Figure 8Q-R)**. This clarifies the hierarchical relationship between baseline immune priming and pyroptosis-amplified memory. While the IBV chassis establishes an early-warning baseline, the pyroptosis-released HMGB1 acts as a potent secondary immunostimulant that profoundly elevates this baseline. Furthermore, although the depletion of $CD8^+$ T cells and NK cells significantly attenuated the antitumor efficacy of TP-IBV, the tumor burden in these depleted groups remained notably lower than in the PBS control **(Figure 8L-N)**. This indicates that additional innate immune populations, particularly tissue-resident myeloid cells, contribute to the residual tumor control. This observation is highly consistent with the massive infiltration and repolarization of $iNOS^+$ tumor-associated macrophages (TAMs) observed within the tumor bed **(Figure 8C)**. Therefore, the pyroptosis-released DAMPs, particularly HMGB1, exert a dual function. Locally, they reprogram macrophages toward a tumoricidal M1-like phenotype, while systemically, they amplify central trained immunity in the bone marrow. To summarize, we propose a comprehensive working model, as illustrated in **Figure 9**, wherein the TP-IBV

platform orchestrates a bidirectional cascade from local immunogenic cell death to systemic central trained immunity.

Context-dependent trained immunity and the role of diverse PAMPs. The functional consequences of trained immunity are highly context-dependent. A recent study revealed that in knee osteoarthritis (KOA), HMGB1 drives a pathogenic trained immunity in circulating monocytes, exacerbating synovial inflammation[44]. This contrasts sharply with our findings. In autoimmune-driven inflammation, HMGB1-induced trained immunity acts as a vicious engine of tissue destruction. In our tumor model, however, HMGB1 released from *in situ* pyroptosis functions as a powerful immune adjuvant that amplifies antitumor memory. This dichotomy highlights the double-edged nature of trained immunity and underscores why it is critical to confine HMGB1 release to the TME. Our TP-IBV design achieves this through tumor-targeted enrichment and uPA-responsive localized release, effectively avoiding systemic, nonspecific HMGB1 exposure while preserving its adjuvant function locally.

Furthermore, the mechanism by which our attenuated vesicles induce trained immunity highlights the functional decoupling of detoxification from adjuvant activity. Rather than attributing the immunostimulatory effects solely to LPS, our data suggest that non-LPS bacterial components are sufficient to establish baseline trained immunity even in a significantly low-endotoxin background. This aligns with, and is strongly supported by, a recent breakthrough study that showed co-administration of BCG and bacterial lipoproteins (BLP) induces durable trained immunity via metabolic-epigenetic rewiring (the lactate-KAT2B-H3K18la axis) in CCR5hi monocytes[63]. In our study, although the *ClearColi* IBV platform has drastically reduced TLR4-activating endotoxin, it retains other potent PAMPs, such as lipoproteins and flagellin. These residual components likely serve as the primary inducers that establish the baseline central trained immunity we observed **(Figure 2)**. Importantly, our TP-IBV design then leverages localized tumor pyroptosis to release HMGB1, a powerful secondary amplifier of this pre-established baseline memory **(Figure 8Q-R)**. Combining the mechanistic insights from the BCG+BLP study with our tumor-targeted platform opens new avenues for rationally designing customized PAMP combinations through synthetic biology. By fine-tuning the specific non-LPS PAMPs retained on the engineered vesicles, we may further optimize the magnitude and durability of the innate immune memory while maintaining an excellent systemic safety profile.

Translational outlook and therapeutic potential. The TP-IBV platform represents a highly engineered modular system with considerable clinical translation potential. The surface display and responsive release modules allow for the rapid substitution of functional modules, such as targeting high concentrations of reactive oxygen species or alternative immune checkpoints. This flexibility addresses microenvironmental heterogeneity across tumor types. Moreover, the production process relies on *E. coli* fermentation, making it less costly than mammalian cell-based antibody manufacturing. While similar to recent findings on how distal inflammatory signals influence bone marrow hematopoietic output in chronic inflammation [64], this represents a novel application of this model in designing antitumor immunotherapy.

By precisely directing the double-edged sword of trained immunity toward host antitumor defense, TP-IBV provides a new theoretical framework and a practical engineered solution for overcoming multi-layered immunosuppression in solid tumors.

Limitations of the study

Despite this study's significant mechanistic and therapeutic findings, several limitations remain and warrant further investigation. First, although we showed that IBV can induce central immune training in the bone marrow and exert sustained antitumor effects 30 days later **(Figure 2)**, the underlying molecular mechanisms of this trained immunity, particularly epigenetic and metabolic reprogramming, remain incompletely elucidated. Second, this study primarily utilized subcutaneous tumor xenograft models (MC38 and 4T1). Although the 4T1 orthotopic model partially simulates metastasis, we have not yet validated therapeutic efficacy in more clinically relevant patient-derived xenograft (PDX) models or genetically engineered spontaneous tumor models. Variations in tumor stroma composition, baseline immune infiltration, and TGF-β abundance across these models may affect TP-IBV generalizability. Finally, this study identifies HMGB1 as a key molecular messenger linking pyroptosis to immune priming; however, the specific transport pathway by which HMGB1 crosses the circulatory system and acts on hematopoietic progenitor cells after its release from the tumor tissue remains an unresolved mechanistic gap. Furthermore, as the aforementioned KOA study [44], indicates, HMGB1-induced trained immunity may exert context-dependent dual roles in different pathological settings. This highlights the need to evaluate the safety boundaries of long-term TP-IBV application across a broader range of disease models.

MATERIALS AND METHODS

Cell Lines and Animals. The mouse colon cancer MC38 cells and melanoma B16F10 cells were purchased from the American Type Culture Collection (ATCC). The murine 4T1 mammary carcinoma cell line is a 6-thioguanine-resistant cell line obtained from 410.4 tumor lines without mutagenesis screening. These cells were provided by the Chinese Academy of Sciences cell bank. All cells were cultivated in Roswell Park Memorial Institute (RPMI) 1640 media (Servicebio), supplemented with 10% FBS (Gibco) and 1% penicillin–streptomycin (Gibco), at 37°C in 5% CO_2 . Female C57BL/6 mice and BALB/c mice (6–8 weeks of age) were procured from SPF Biotechnology Co., Ltd. (Beijing, China). Furthermore, all mice were maintained in a specific pathogen-free environment. The animal operations in question complied with established ethical standards and had received the requisite approval from the Animal Care and Welfare Ethics Committee of the Institute of Medical Biology, Chinese Academy of Medical Sciences (ethics number: DWSP202505015).

Plasmid Construction. The extracellular domain (amino acids 24–166) of murine TGFβRII was fused to the C-terminus of ClyA via a $(GGGGS)_4$ linker[22, 24]. A GGGGS linker followed by a six-Histidine (HHHHHH) tag was further appended to the C-terminus of the fusion protein to facilitate protein detection, resulting in the ClyA-TGFβRII fusion protein. For the other construct, the amino acid sequence of a

PD-L1 nanobody (nb)[57] was fused to the C-terminus of ClyA using a $(GGGGS)_2$ linker along with a uPA cleavage site $(LSGRSDNH)_3$[27], and a Flag tag was added at the C-terminus, yielding the fusion protein ClyA-uPA-PD-L1 nb. The corresponding nucleotide sequences were codon-optimised and synthesised by Genscript Biotech Corporation (Nanjing, China). Each gene was individually cloned into the pET-24a(+) plasmid. In addition, both genes were co-cloned into the dual-expression plasmid vector pRSF-Duet-1.

IBV and engineered IBV Preparation. IBV and engineered IBV were produced following established methods. Briefly, the recombinant plasmid was electroporated into *ClearColi*® BL21(DE3) cells (Biosearch Technologies, USA). Transformed cells were grown in Luria-Bertani (LB) medium (containing 1% tryptic soy broth, 0.5% yeast extract, and 1% NaCl) at 37°C with shaking at 220 rpm until the optical density at 600 nm (OD600) reached 0.6. Protein expression was then induced by adding 1 mmol/L isopropyl β-D-1-thiogalactopyranoside (IPTG, Solarbio) and incubating the culture at 28°C with shaking at 220 rpm for 20 hours. The bacterial cells were collected by centrifugation (14,000 × g, 30 min, 4°C). The pellet was resuspended in approximately 300 mL of Hank's Balanced Salt Solution (HBSS) and subjected to three cycles of high-pressure homogenization using an APV-2000 homogenizer at 1200 bar and 4°C. After homogenization, the lysate was centrifuged (10,000 × g, 30 min, 4°C) to remove cell debris. The supernatant was further processed by ultracentrifugation (100,000 × g, 30 min, 4°C) to pellet the expressed engineered IBV particles. The resulting pellet was resuspended in HBSS and purified using an OptiPrep™ (Sigma) density gradient by centrifugation at 130,000 × g for 4 hours at 4°C. The target fraction was collected and passed through a 0.22 μm pore-size membrane filter (Millipore) to remove any residual bacterial or particulate contaminants. The protein concentration of the purified samples was quantified with a Micro BCA Protein Assay Kit (Servicebio). Finally, both the IBV and engineered IBV preparations were aliquoted and stored at -80°C until use in subsequent cellular and animal studies.

Identification and Characterisation of Engineered IBV. To verify the expression of the target protein in IBV, we performed SDS-PAGE and Western blot (WB) analysis. Purified engineered IBV samples were separated by 12% SDS-PAGE gel electrophoresis and transferred to PVDF membranes (Millipore). Primary antibodies used were mouse anti-His tag monoclonal antibody (Abcam) or mouse anti-Flag tag monoclonal antibody (Beyotime), with HRP-labelled anti-mouse IgG (Beyotime) as the secondary antibody. Protein band purity was assessed using ImageLab software (Bio-Rad, version 6.0.1). IBV and engineered IBV morphology were examined by transmission electron microscopy (TEM): 10 μL of the sample was spotted onto a carbon-coated copper grid, counterstained with 0.75% (w/v) uranyl acetate, dried for 30 minutes, and imaged using a Hitachi TEM. Additionally, the particle size distributions of IBV and engineered IBV were determined using dynamic light scattering with a Zetasizer Nano ZS particle size analyser (Malvern Instruments, UK).

For stability assessment of engineered IBV, T-IBV samples underwent two distinct treatment protocols: storage at -20°C, 4°C, or 25°C for 2 weeks, or 1 to 5 freeze-thaw cycles. The freeze-thaw procedure involved immersing samples in liquid nitrogen for 5 minutes, then transferring them to a 42°C water bath until complete thawing. Dynamic light scattering (DLS) was then employed to assess IBV particle size distribution and Polydispersity Index (PDI), evaluating nanostructure stability. Additionally, T-IBV stored in 10% FBS (Gibco) was analysed via TEM and DLS to evaluate nanostructure stability in serum. For endotoxin detection, the LAL assay was performed using a commercially available kit (GenScript) according to the manufacturer's instructions.

Generation of BMDCs and BMDMs. Bone marrow-derived dendritic cells (BMDCs) and macrophages (BMDMs) were generated from the femurs and tibias of C57BL/6 mice. Briefly, flushed bone marrow cells were passed through a 70 μm cell strainer, treated with red blood cell lysis buffer (BioLegend), and cultured. For BMDC differentiation, cells were cultured in complete RPMI-1640 medium supplemented with 15 ng/mL GM-CSF (MedChemExpress) and 20 ng/mL IL-4 (MedChemExpress), with half the medium replaced every 2 days, and harvested on day 7. For BMDM differentiation, cells were cultured in DMEM containing 10% FBS and 10 ng/mL murine M-CSF (MedChemExpress), with half the medium replaced every 2 days, and were harvested on day 7 for subsequent use.

Evaluation of an *in vitro* trained immunity model using BMDCs and BMDMs. BMDCs and BMDMs were adjusted to a live cell concentration of 5×10^5 cells/mL and cultured at 37°C in 5% CO_2 . Subsequently, 5 μg of IBV/T-IBV derived from *ClearColi* and 5 μg of IBV/T-IBV derived from *E. coli* were added to the BMDCs and BMDMs, respectively. For experiments in which HMGB1 induced trained immunity in BMDMs, mouse HMGB1 (MedChemExpress, Cat#HY-P73104A) was added to BMDMs at final concentrations of 0.1, 1, 10, and 100 μg/mL. After 24 hours of stimulation, the culture medium was replaced with complete RPMI-1640 or DMEM medium. After a 6-day rest period, the cells were restimulated with LPS (final concentration 10 ng/mL, Sigma) for 24 hours, followed by centrifugation (300× g, 5 min) to collect the supernatant. Untrained BMDCs or BMDMs were used as controls. Cytokine concentrations (IL-6, IL-1β, TNF-α, and IFN-γ) in the supernatant were measured using ELISA kits (Thermo Fisher) according to the manufacturer's instructions.

Evaluation of IBV-Induced *In Vivo* Trained Immunity. To evaluate IBV-induced in vivo trained immunity and its effects on central and peripheral immune organs, as well as tumor suppression, we administered a 50 μg intravenous injection of IBV derived from *ClearColi*. Thirty days later, they underwent secondary LPS stimulation, immunohistological sampling, and MC38 tumor implantation, respectively. In the LPS secondary stimulation experiment, mice were administered LPS (Sigma, 10 μg/mouse) intraperitoneally, and serum was collected 4 hours later. IL-6, IL-1β, TNF-

α, and IFN-γ were measured according to the instructions for the Thermo Fisher ELISA kit. For the immunohistological assessment, spleen, inguinal lymph nodes, lung tissue, and bone marrow were collected from the mice. The spleen was ground using a 70-μm cell sieve (NEST), and splenic immune cells were isolated using the mouse immune cell isolation buffer (Dakewe, Cat. No. #7211011) according to the instructions; erythrocytes were lysed using erythrocyte lysis buffer (BioLegend, Cat. No. #420302), resuspended in RPMI-1640 medium (Biological Industries), and counted. Lung tissue was minced and suspended in 0.5 mL of 1 mg/mL collagenase solution (Sigma, Cat. No. # 9001-12-1), digested at 37°C and 200 rpm for 30 min, filtered through a 70-μm cell strainer, and then immune cells were isolated using isolation buffer according to the manufacturer's instructions. Inguinal lymph nodes were directly ground through a 70-μm cell strainer and counted. Bone marrow cells were obtained by flushing the femur and tibia, filtered through a 70 μm filter membrane, treated with erythrocyte lysis buffer, and cultured; BMDM differentiation was induced in DMEM containing 10% FBS and 10 ng/mL mouse M-CSF (MedChemExpress). Half of the medium was replaced every two days, and cells were harvested and counted on day 7. Subsequently, immune cells from the aforementioned tissue sources and BMDMs were seeded at 5×10^5 cells per well and stimulated with LPS at a final concentration of 10 ng/mL for 24 hours. The supernatant was collected, and IL-6, IL-1β, TNF-α, and IFN-γ were detected according to the instructions of the Thermo Fisher ELISA kit. In the tumor suppression assay, mice were administered 50 μg of IBV derived from ClearColi intravenously. Thirty days later, 5×10^5 MC38 tumor cells (100 μL) were injected subcutaneously into the right dorsal region, and tumor growth was monitored.

T-IBV in vitro specific binding. The binding of TGFβ to T-IBV was detected using a standard ELISA method. Brief steps are as follows: Dilute T-IBV to 10 μg/mL in PBS, and add 100 μL per well to a 90-well ELISA plate (NEST). Incubate overnight at 4°C to coat the 96-well ELISA plate. Concurrently, IBV was coated as a control. The following day, wash the plate three times with washing buffer (PBS containing 0.05% Tween-20). Block the plate at room temperature for 1 hour with PBS containing 2% bovine serum albumin (BSA). After discarding the blocking solution, add the following recombinant proteins: TGFβ1 (Thermo Fisher, Cat#88-8350), TGFβ2 (Biorbyt, Cat#orb779074), and TGFβ3 (Biorbyt, Cat#orb776563) in a 1:2 gradient dilution. Add the diluted samples in duplicate wells and incubate at room temperature for 2 hours. After washing the plate three times, add the corresponding anti-mouse TGFβ1 biotin-conjugated antibody (Thermo Fisher, Cat#88-8350), TGFβ2 biotin-conjugated antibody (Biorbyt, Cat#orb779074), and TGFβ3 biotin-conjugated antibody (Biorbyt, Cat#orb776563) for incubation at room temperature for 1 hour. After washing, incubate with Avidin-HRP at room temperature for 30 minutes. Wash again, then develop color with TMB (Solarbio), and terminate the reaction by adding 1.0 M sulfuric acid. Finally, measure the OD at 450 nm (OD450) with a microplate reader (Thermo Fisher).

Analysis of Differential Expression of TGF-β Subtypes in Colorectal and Breast Cancers. To analyze the expression profiles of different TGF-β subtypes in human colorectal and breast cancers, we downloaded and organized STAR-processed RNA-seq data from the TCGA database (https://portal.gdc.cancer.gov) for the TCGA-COAD (colorectal adenocarcinoma) and TCGA-BRCA (invasive breast carcinoma) projects, respectively; TPM-formatted expression matrices were extracted, and paired samples of normal adjacent tissue and tumor tissue were selected based on sample IDs. Based on characteristics such as data distribution and homogeneity of variance, appropriate statistical methods were selected using the `stats` and `car` packages in R for between-group comparisons; data that did not meet the prerequisites for the corresponding statistical tests were excluded from the analysis. The `ggplot2` package was used to visualize the analysis results. All analyses were performed in R.

***In vivo* and *in vitro* cleavage assays of P-IBV.** uPA enzyme (MedChemExpress, Cat#HY-P73467) at a concentration of 100 μg/mL was added to pre-prepared P-IBV (40μg). The uPA enzyme was added in volumes of 2, 5, and 10 μL, resulting in a final reaction volume of 20μL in each case. A control group without uPA was included. The mixture was reacted at 37°C for 24 hours, after which samples were collected for SDS-PAGE and Western blotting (WB) using anti-mouse Flag antibody (Beyotime). For in vivo tumor cleavage validation of P-IBV, mice bearing 4T1 tumors (tumor volume ~75 mm^3) received an intratumoral injection of 20 μg P-IBV. Two hours post-administration, mice were euthanized, and tumor tissue was collected and immediately homogenized in RIPA lysis buffer (Servicebio) containing 1 mM PMSF and a protease inhibitor mixture (Servicebio). The homogenate supernatant was rapidly frozen in liquid nitrogen and stored at -80°C for subsequent Western blotting analysis.

***In Vivo* Distribution and Safety Assessment of T-IBV.** IBV and T-IBV were incubated with Dil (Beyotime, C1036) at 37°C for 1 hour. Free Dil was removed by ultracentrifugation (100,000 × g, 30 min, 4°C). MC38 tumor-bearing mice (tumor volume ~60 mm^3) received intravenous injections of 50 μg IBV and T-IBV, respectively. Dil fluorescence signals were detected using an in vivo imaging system (in vivo FX PRO, Bruker). Tumor tissues, major organs, and serum were collected at designated time points for fluorescence imaging and analysis. 120 hours after injection of Dil-labeled T-IBV, tumors were harvested and sectioned for frozen sections. Immunofluorescence staining for mouse TGF-β was performed using an anti-TGF-β antibody (Servicebio, Cat#GB115739) followed by DAPI staining. The corresponding fluorescent signals were then observed using a fluorescence confocal microscope, and images were captured. For preliminary safety assessment of T-IBV, 6–8-week-old female C57BL/6 mice received intravenous injections of T-IBV at doses of 50, 100, 200, or 500 μg total protein on Day 0. Serum samples were collected and mouse body weights measured at designated time points. Serum cytokines (TNFα, IL-6, IL-1β, IFN-γ) were measured using ELISA kits (Thermo Fisher) according to the manufacturer's instructions. Additionally, major organs were

harvested on day 7, H&E-stained, and analyzed for potential injury and immune cell infiltration. Furthermore, T-IBV derived from E. coli BL21 (200 μg per mouse) was administered intravenously as a control, and body weight was monitored; organs were collected.

Evaluation of T-IBV/TP-IBV Antitumor Effects. To assess antitumor efficacy of T-IBV and determine an appropriate dosage for solid tumors, 5×10^5 MC38 tumor cells (100 μL) were subcutaneously inoculated into the right dorsal region of 6- to 8-week-old female C57BL/6 mice to establish a subcutaneous xenograft model. When the tumor volume reached approximately 60 mm^3, mice were randomly divided into 5 groups. Designated formulations (PBS, 50 μg IBV, 50 μg T-IBV, 100 μg T-IBV, 200 μg T-IBV) were administered via tail vein injection to C57BL/6 mice every 3 days for a total of 3 injections. Subcutaneous 4T1 breast cancer models and in situ mammary carcinoma models were established by inoculating 1×10^5 4T1 tumor cells (100 μL) subcutaneously into the right dorsal region of 6–8-week-old female BALB/c mice or into the second mammary fat pad of female BALB/c mice (50 μL), respectively. When tumor volume reached approximately 50 mm^3, administer 100 μg T-IBV intravenously every 3 days for a total of 3 injections. Subsequently, monitor tumor volume every 3 days using the following formula: tumor volume (mm^3) = 0.5 × length × $(width)^2$. Collect tumors, spleens, and lungs at designated time points for antitumor efficacy assessment. The antitumor effects of TP-IBV were evaluated in established MC38 and 4T1 subcutaneous xenografts following the above immunisation protocol, with the following doses administered: T-IBV (100 μg), P-IBV (100 μg), TP-IBV (100 μg), P-IBV (100 μg) + anti-PD-L1mAb (200 μg, B7-H1, Clone: 10F.9G2, BioXcell). At the experimental endpoint, tumors, spleens, and lungs were collected for subsequent immunological evaluation of antitumor effects.

Depletion of NK cells, CD8+ T cells *in vivo*. 4T1 tumor cells (1×10^5 cells per mouse) were subcutaneously implanted into female BALB/c mice. Cell subsets were depleted via intraperitoneal antibody injections starting one day prior to TP-IBV treatment. CD8+ T cells were treated with anti-mouse CD8 antibody (Clone: 2.43, BioXcell, Cat#BE0061). Each mouse received 200 μg of monoclonal antibody per injection, administered every two days to maintain continuous depletion of immune cells. NK cells were treated with anti-Asialo-GM1 Antibody (Clone: Poly21460, Biolegend, Cat#146002) at 50 μL per injection, administered every 3 days. NK cell and CD8+ T cell depletion was confirmed by spleen flow cytometry. All tumor volumes were measured using electronic callipers.

Antibody Staining and Flow Cytometry Analysis. For MC38 and 4T1 tumor models, the analysis methods for immune cell responses in tumor tissues and spleens followed previous literature[22, 65]. Spleens were placed in a 70 μm cell mesh (NEST) and separated using mouse lymphocyte isolation buffer (Dakewe, Cat#7211011) according to the manufacturer's instructions to isolate splenic lymphocytes. Red blood cells were lysed using red blood cell lysis buffer (Biolegend, Cat#420302), and the

isolated splenocytes were resuspended in RPMI-1640 medium (Biological Industries) for counting. To isolate lymphocytes from tumor tissue, the tumor was dissected, minced with scissors, and suspended in 1 mL of collagenase solution (Sigma, Cat#9001-12-1) at 1 mg/mL. The tissue suspension was digested for 45 minutes at 37°C on an incubator set to 200 rpm. The digested tumor tissue was passed through a 70 μm cell mesh (NEST), and tumor-infiltrating lymphocytes were isolated using mouse lymphocyte isolation buffer (Dakewe, Cat#7211011) according to the manufacturer's protocol. Red blood cells were lysed using red blood cell lysis buffer (Biolegend, Cat#420302). The isolated cells were resuspended in RPMI-1640 medium (Biological Industries) and counted. 1×10^6 lymphocytes were seeded into 96-well U-bottom plates (Corning) and stained with various combinations of flow cytometry antibodies, including: Brilliant Violet 510™ anti-mouse CD45 (Biolegend, Cat#103138), FITC anti-mouse CD3 (Biolegend, Cat#100204), FITC anti-mouse/human CD11b (Biolegend, Cat#101206), APC anti-mouse F4/80 (Biolegend, Cat#123116), Brilliant Vio let 421™ anti-mouse CD86 (Biolegend, Cat#105032), APC anti-mouse CD11b (Biolegend, Cat#101212), PE anti-mouse Ly-6G/Ly-6C (Gr-1) (Biolegend, Cat#108408), Brilliant Violet 421™ anti-mouse NK1.1 (Biolegend, Cat#108731), APC anti-mouse CD8a (Biolegend, Cat#100712), PE anti-mouse CD279 (PD-1) (Biolegend, Cat#135206), Brilliant Violet 421™ anti-mouse CD366 (Tim-3)(Biolegend, Cat#134019), PE anti-mouse/human CD44 (Biolegend, Cat#103008), and PE/Cyanine7 anti-mouse CD62L (Biolegend, Cat#161214). All antibodies were diluted according to the manufacturer's recommended concentrations. Following surface staining, intracellular IFN-γ was stained to analyze antigen-specific effector cell responses. When analyzing antigen-specific T cell responses in the MC38 tumor model, 10 μL of MC38 neoantigen peptide Adpgk (ASMTNMELM, synthesized by Shanghai Sangon Biotech Co., Ltd., purity >98%) at an initial concentration of 1 mg/mL was added to the cells. In the 4T1 tumor model, 10μL of Zfp142 neoantigen peptide (CPQTHAVVL, synthesized by Shanghai Sangon Biotech Co., Ltd., purity >98%) at an initial concentration of 1 mg/mL was added to the cells (10 μL per well). Subsequently, 5 μg/mL brefeldin A (BioLegend, Cat#420601) was added after 3 hours of stimulation to promote intracellular cytokine accumulation. Following surface staining, cells were fixed/permeabilized using Fixation Buffer (BioLegend, Cat#420801) and Intracellular Staining Perm Wash Buffer (BioLegend, Cat#421002). Following surface staining, intracellular IFN-γ and CD206 were stained. The procedure was as follows: First, cells were fixed with 1×Fixation Buffer (BioLegend, Cat#420801) for 20 minutes. Subsequently, cells were resuspended in 1× Permeabilization Wash Buffer (BioLegend, Cat#427706), followed by staining with the corresponding antibodies. Intracellular cytokine staining was performed using PE/Cyanine7 anti-mouse CD206 (Biolegend, Cat#141720) and PE anti-mouse IFN-γ (Biolegend, Cat#505808). Finally, cells were analyzed using a CytoFLEX flow cytometer (Beckman Coulter) and processed with FlowJo software (Tree Star Inc.).

Transcriptomic analysis. Female BALB/c mice bearing 4T1 tumors received treatment according to the specified protocol. Five days after the final dose, tumor

tissue was collected, rapidly frozen in liquid nitrogen, and shipped to Gene Denovo Biotechnology Co., Ltd. (Guangzhou, GENE DENOVO) for total RNA extraction and library preparation. Gene Denovo Biotechnology Co. (Guangzhou, China) performed RNA sequencing using the Illumina NovaSeq 6000. After sequencing, the data underwent further validation and filtering to obtain clean reads, which were then aligned to the mouse reference genome version Ensembl-release115 from the Ensembl database. We analyzed gene expression levels for each sample and treatment group using the Bioinformatics Cloud Platform (https://www.omicsmaster.com/).

Hematoxylin and Eosin (H&E) staining and picrosirius red staining. The collected tumor and lung tissues were fixed in 4% paraformaldehyde (Servicebio), followed by routine dehydration, clearing, and paraffin embedding to prepare 4-μm-thick sections. After dewaxing and rehydration, the sections were stained with hematoxylin and eosin (H&E) and examined under a light microscope, with images captured. For picrosirius red staining, a modified Picrosirius Red staining kit (Servicebio, Cat#G1078) was used according to the manufacturer's instructions. After staining, the slides were dehydrated and mounted. The stained sections were imaged under a microscope; under light microscopy, collagen fibers appeared red against a yellow background; under polarized light, Type I collagen appeared as coarse, orange-yellow or bright red fibers, while Type III collagen appeared as fine, green fibers.

Immunohistochemistry. Immunohistochemical staining with anti-Ki67 and anti-α-SMA was performed according to our laboratory's established protocol. After dewaxing the paraffin sections, the tissue sections were immersed in EDTA antigen retrieval buffer (pH 8.0, Servicebio) for antigen retrieval. After blocking, the sections were incubated separately with anti-Ki67 antibody (Servicebio, Cat# GB111141) and anti-α-SMA antibody (Servicebio, Cat# GB111364) at 4 °C overnight. After washing on a decolorizing shaker, add HRP-labeled secondary antibody matching the primary antibody's species dropwise to cover the tissue, then incubate at room temperature for 50 minutes. Develop the signal with diaminobenzidine (DAB) substrate, then observe and capture images under a light microscope.

Immunofluorescence of Tumor Tissue. Immunofluorescence staining of tumor tissue was performed according to the established methods of this laboratory[22, 52, 65]. Tumor tissue was fixed in 4% paraformaldehyde (Servicebio, Cat#G1101) and processed into paraffin sections. The sections were immersed in EDTA antigen retrieval buffer for antigen retrieval, followed by incubation with anti-CD8 antibody (Servicebio, GB13429), anti-granzyme B antibody (Abcam, ab317458), anti-Foxp3 antibody (Servicebio, GB112325), anti-F4/80 antibody (Servicebio, GB112325), anti-Ki67 antibody (Servicebio, GB111499), anti-CD4 antibody (Servicebio, GB15064), anti-GSDME antibody (Servicebio, GB150167), anti-GSDMD antibody (Abcam, ab219800), anti-uPA antibody (Servicebio, GB11958) or anti-iNOS antibody (Servicebio, GB11119) and incubated overnight at 4 °C. Subsequently, Alexa Fluor

488-, Alexa Fluor 594-, or Cy3-labeled secondary antibodies were added and incubated at room temperature for 1 h. Add DAPI (Servicebio, G1012) dropwise and incubate at room temperature for 10 minutes to stain the cell nuclei. For the TUNEL assay, sections were first treated with proteinase K (Servicebio, G1205) and then permeabilized with 0.1% Triton. Next, sections were incubated with the TUNEL reaction mixture (Servicebio, G1504)—prepared at a TdT enzyme: dUTP: buffer ratio of 1:5:50—in a 37 ° C incubator for 2 hours. Finally, the cell nuclei were stained with DAPI (Servicebio, G1012). All of the fluorescently stained sections were observed and imaged using a fluorescence microscope (Nikon Eclipse C1).

***In vitro* assay for evaluating immunogenic cell death (ICD) in tumor cells.**
4T1 tumor cells were incubated at 1×10^6 cells per well with 5 μg of vesicles derived from T-IBV, P-IBV, or TP-IBV for 24 h. Blank control and TP-IBV + GSDMD inhibitor Necrosulfonamide (MedChemExpress, HY-100573) groups were included to evaluate the effects on cell death. After 24 h of incubation, add 1 μL SYTOX Green cell staining solution (Invitrogen, Cat# S7020) to each well. The samples were incubated at room temperature in the dark for 30 min, and the cell death status in each treatment group was observed under a fluorescence microscope, with images captured. Four fields of view were randomly selected to analyze the proportion of green-fluorescent cells and quantify the cell death rate. At the same time, cell supernatants were collected, and ATP release and LDH activity in the supernatants were measured using an ATP assay kit (Abbkine, Cat# KTB1016) and a lactate dehydrogenase (LDH) activity assay kit (Abbkine, Cat# KTB1110).

Western blotting was used to verify GSDME cleavage. In vitro experiments involved incubating 4T1 tumor cells with 5 μg of vesicles derived from T-IBV, P-IBV, or TP-IBV for 24 h, with a blank control group and a TP-IBV+NSA group. After 24 h of incubation, cell samples were lysed in RIPA buffer containing 1% (v/v) protease inhibitor mixture (MedChemExpress). In the in vivo experiments, tumor tissue was collected 2 days after the second dose in the designated treatment groups. The tissue was treated with RIPA lysis buffer (MedChemExpress, HY-K1001), a 1% protease inhibitor mixture (MedChemExpress, HY-K0010), 1% phosphatase inhibitor (MedChemExpress, HY-K0022), and PMSF at a final concentration of 1 mM (MedChemExpress, HY-B0496). The samples were homogenized and lysed on ice for 30 minutes, then centrifuged at 10,000 × g for 10 minutes, and the supernatant was collected. Protein concentrations in each sample were determined using the BCA Protein Concentration Assay Kit (Beyotime Biotechnology) according to the kit instructions. Subsequently, whole-cell lysates or cell supernatants were separated by SDS-PAGE and transferred to a PVDF membrane (Millipore). After incubating the membrane with the GSDME rabbit monoclonal antibody (Abcam, ab215191), it was incubated with HRP-labeled goat anti-rabbit secondary antibody (Abcam, ab6721) at room temperature for 2 hours. The membrane was washed three times with 1 × TBST at room temperature for 10 minutes each, then exposed and visualized. All antibodies were diluted and used at the manufacturer-recommended concentrations.

Evaluation of In Vivo GSDMD Inhibition and Central Trained Immunity. GSDMD inhibitor disulfiram (MedChemExpress, HY-B0240) was administered intraperitoneally to 4T1-tumor-bearing mice at a dose of 50 mg/kg once daily. At the

end of the experiment, bone marrow-derived macrophages (BMDMs) were isolated from the PBS, TP-IBV, and TP-IBV+Disulfiram groups according to the methods described above. BMDMs were cultured in DMEM containing 10% FBS and 10 ng/mL mouse M-CSF (MedChemExpress, HY-P7085), with medium changes every 2 days (half volume), and harvested on day 7 for subsequent experiments. BMDMs were adjusted to a live cell concentration of 5×10^5 cells/mL and cultured at 37 °C in a 5% CO_2 atmosphere. BMDMs were restimulated for 24 hours with LPS (final concentration 10 ng/mL, Sigma), Pam3CSK4 (final concentration 10 μg/mL, MedChemExpress), and 4T1 tumor cell lysate (1×10^5 cells per well), followed by centrifugation at 300 × g for 5 minutes to collect the supernatant. The concentrations of IL-6 and TNF-α in the supernatant were measured using an ELISA kit (Thermo Fisher) according to the manufacturer's instructions.

Enzyme-Linked Immunospot Assay (ELISPOT). For the 4T1 tumor model, isolated tumor-infiltrating lymphocytes were seeded onto ELISPOT plates at 3×10^5 or 1×10^5 cells per well. Each well was treated with either 5μL of the 4T1 neoantigen peptide Zfp142 (CPQTHAVVL,synthesized by Shanghai Sangon Biotech Co., Ltd., purity >98%) at an initial concentration of 1 mg/mL. After gentle mixing, the plates were incubated at 37℃ in a 5% CO2 incubator. After gentle mixing, the cells were incubated at 37℃in a 5% CO2 incubator. Cells treated with PMA (Dakewe, Cat#2030421,10μL per well) or PBS served as positive and negative controls, respectively. After 36 hours, IFN-γ was detected using an IFN-γ enzyme-linked immunosorbent assay (ELISA) according to the manufacturer's protocol (MabTech, Cat#3321-4AST). After allowing the microplate to dry naturally in a cool place, the colorimetric spots were counted using an ELISA reader system (AID), and the spot data were recorded for statistical analysis.

Statistical Analysis. All statistical analyses were performed with GraphPad Prism (version 10.0). Quantitative data are presented as mean ± standard deviation (SD). Differences in tumor growth dynamics across multiple time points were assessed by two-way ANOVA. For comparisons involving more than two groups, one-way ANOVA followed by Tukey's post hoc test was utilized. A two-tailed paired Student's t-test was employed for direct comparisons between two groups. Survival outcomes were evaluated using the Log-rank test. Statistical significance is indicated as follows: ns (not significant), *$p < 0.05$, **$p < 0.01$, ***$p < 0.001$, and ****$p < 0.0001$.

Acknowledgements

Author contributions

P.Z., S.B., and T.Y. contributed equally to this work. P.Z. and Y.M. conceived and designed the research. P.Z. led the overall project, including molecular, cellular, and animal experiments; analyzed the research and RNA-seq data; and drafted the manuscript. S.B. prepared and characterized IBV, T-IBV, and TP-IBV; performed ELISPOT assays, monitored tumor growth curves, and detected cytokines. T.Y. constructed the tumor models and trained immunity evaluation models, and performed in vitro cell experiments, flow cytometry staining, and data collection.

Y.Y., X.Y., Y.L., Y.T., X.Z., S.L., Q.L., H.B., and X.Y. participated in the animal experiments and lymphocyte separation. Y.M. provided guidance and supervision for this study and reviewed the manuscript. All authors read and approved the final article. All authors provided written permission to the corresponding author to be named in the article.

Competing interests

The authors declare no competing financial interest.

Acknowledgments

This work was financially supported by the National Natural Science Foundation of China (Grant No. 82603585 to P.Z. and No. 82471865 to Y.M.), the Major Project in Basic Research of Yunnan Province (Grant No. 202401 BC070009 to Y.M.), the Fundamental Research Funds for the Central Universities, Peking Union Medical College (Grant No. 3332025071 to P.Z.), the China Postdoctoral Science Foundation (Grant No. 2026M791496 to P.Z.), the Postdoctoral Fellowship Program of CPSF (Grant No. GZB20260881 to P.Z.), and the Yunnan Fundamental Research Projects (Grant No. 202601CF070103 to P.Z.).

Data and materials availability

All data relevant to this study are included in the article and its supplementary materials. The plasmids and T-IBV, P-IBV, and TP-IBV samples constructed in this study are available upon request. To obtain these materials, please contact Y.M. after signing a Material Transfer Agreement.

Supplementary Materials

Supplementary Information includes Figure S1 to Figure S17.

REFERENCES AND NOTES

1. Ramos-Casals M*, et al.* Immune-related adverse events of checkpoint inhibitors. *Nat Rev Dis Primers* **6**, 38 (2020).
2. de Miguel M, Calvo E. Clinical Challenges of Immune Checkpoint Inhibitors. *Cancer Cell* **38**, 326-333 (2020).
3. Zappasodi R, Merghoub T, Wolchok JD. Emerging Concepts for Immune Checkpoint Blockade-Based Combination Therapies. *Cancer Cell* **33**, 581-598 (2018).
4. Nixon BG, Gao S, Wang X, Li MO. TGFbeta control of immune responses in cancer: a holistic immuno-oncology perspective. *Nat Rev Immunol* **23**, 346-362 (2023).
5. Shi X*, et al.* TGF-β signaling in the tumor metabolic microenvironment and targeted therapies. *Journal of hematology & oncology* **15**, (2022).
6. Liu S, Ren J, Ten Dijke P. Targeting TGFbeta signal transduction for cancer therapy. *Signal Transduct Target Ther* **6**, 8 (2021).

7. Groeneveldt C, van Hall T, van der Burg SH, Ten Dijke P, van Montfoort N. Immunotherapeutic Potential of TGF-beta Inhibition and Oncolytic Viruses. *Trends Immunol* **41**, 406-420 (2020).
8. Batlle E, Massague J. Transforming Growth Factor-beta Signaling in Immunity and Cancer. *Immunity* **50**, 924-940 (2019).
9. Mariathasan S*, et al.* TGFβ attenuates tumour response to PD-L1 blockade by contributing to exclusion of T cells. *Nature* **554**, 544-548 (2018).
10. Lan Y*, et al.* Simultaneous targeting of TGF-β/PD-L1 synergizes with radiotherapy by reprogramming the tumor microenvironment to overcome immune evasion. *Cancer Cell* **39**, 1388-1403.e1310 (2021).
11. Ciardiello D, Elez E, Tabernero J, Seoane J. Clinical development of therapies targeting TGFbeta: current knowledge and future perspectives. *Ann Oncol* **31**, 1336-1349 (2020).
12. Tauriello DVF, Sancho E, Batlle E. Overcoming TGFbeta-mediated immune evasion in cancer. *Nat Rev Cancer* **22**, 25-44 (2022).
13. Yi M, Zheng X, Niu M, Zhu S, Ge H, Wu K. Combination strategies with PD-1/PD-L1 blockade: current advances and future directions. *Mol Cancer* **21**, 28 (2022).
14. Ravi R*, et al.* Bifunctional immune checkpoint-targeted antibody-ligand traps that simultaneously disable TGFbeta enhance the efficacy of cancer immunotherapy. *Nat Commun* **9**, 741 (2018).
15. Mariathasan S*, et al.* TGFbeta attenuates tumour response to PD-L1 blockade by contributing to exclusion of T cells. *Nature* **554**, 544-548 (2018).
16. Lan Y*, et al.* Enhanced preclinical antitumor activity of M7824, a bifunctional fusion protein simultaneously targeting PD-L1 and TGF-β. *Sci Transl Med* **10**, (2018).
17. Yi M, Li T, Wu K, Dai Z. From M7824 to SHR-1701: lessons for dual PD-L1/TGF-β targeting. *J Immunother Cancer* **14**, (2026).
18. Fan W, Yung B, Huang P, Chen X. Nanotechnology for Multimodal Synergistic Cancer Therapy. *Chem Rev* **117**, 13566-13638 (2017).
19. Singh H*, et al.* Engineering combination nanomedicines to overcome cancer resistance. *RSC Adv* **16**, 5128-5167 (2026).
20. Zhuang L, Lian Y, Zhu T. Multifunctional gold nanoparticles: bridging detection, diagnosis, and targeted therapy in cancer. *Mol Cancer* **24**, 228 (2025).
21. Li X*, et al.* Engineering an Organic Nanoplatform for Augmented Pyroeletroimmunotherapy. *Adv Mater* **36**, e2400756 (2024).
22. Zheng P*, et al.* Engineered Bacterial Biomimetic Vesicles Reprogram Tumor-Associated Macrophages and Remodel Tumor Microenvironment to Promote Innate and Adaptive Antitumor Immune Responses. *ACS Nano* **18**, 6863-6886 (2024).
23. Long Q*, et al.* Engineered bacterial membrane vesicles are promising carriers for vaccine design and tumor immunotherapy. *Adv Drug Delivery Rev* **186**, 114321 (2022).

24. Hua L, *et al.* A Novel Immunomodulator Delivery Platform Based on Bacterial Biomimetic Vesicles for Enhanced Antitumor Immunity. *Adv Mater* **33**, e2103923 (2021).
25. Yang Z, *et al.* RBD-Modified Bacterial Vesicles Elicited Potential Protective Immunity against SARS-CoV-2. *Nano Lett* **21**, 5920-5930 (2021).
26. Toyofuku M, Schild S, Kaparakis-Liaskos M, Eberl L. Composition and functions of bacterial membrane vesicles. *Nat Rev Microbiol*, (2023).
27. Liang J, *et al.* Outer Membrane Vesicle-Based Nanohybrids Target Tumor-Associated Macrophages to Enhance Trained Immunity-Related Vaccine-Generated Antitumor Activity. *Adv Mater* **35**, e2306158 (2023).
28. Liang J, *et al.* Outer Membrane Vesicle-Based Nanohybrids Target Tumor-Associated Macrophages to Enhance Trained Immunity-Related Vaccine-Generated Antitumor Activity. *Adv Mater*, e2306158 (2023).
29. Xie J, Li Q, Haesebrouck F, Van Hoecke L, Vandenbroucke RE. The tremendous biomedical potential of bacterial extracellular vesicles. *Trends Biotechnol*, (2022).
30. Qing S, *et al.* Biomineralized Bacterial Outer Membrane Vesicles Potentiate Safe and Efficient Tumor Microenvironment Reprogramming for Anticancer Therapy. *Adv Mater* **32**, e2002085 (2020).
31. Mamat U, *et al.* Endotoxin-free protein production—ClearColi™ technology. *Nature Methods* **10**, 916-916 (2013).
32. Ziogas A, Bruno M, van der Meel R, Mulder WJM, Netea MG. Trained immunity: Target for prophylaxis and therapy. *Cell Host Microbe* **31**, 1776-1791 (2023).
33. Netea MG, Joosten LAB. Trained innate immunity: Concept, nomenclature, and future perspectives. *J Allergy Clin Immunol* **154**, 1079-1084 (2024).
34. Cirovic B, *et al.* BCG Vaccination in Humans Elicits Trained Immunity via the Hematopoietic Progenitor Compartment. *Cell Host Microbe* **28**, 322-334 e325 (2020).
35. Kleinnijenhuis J, *et al.* Bacille Calmette-Guerin induces NOD2-dependent nonspecific protection from reinfection via epigenetic reprogramming of monocytes. *Proc Natl Acad Sci U S A* **109**, 17537-17542 (2012).
36. Ziogas A, *et al.* Long-term histone lactylation connects metabolic and epigenetic rewiring in innate immune memory. *Cell* **188**, 2992-3012 e2916 (2025).
37. Zhang B, *et al.* Single-cell RNA sequencing reveals induction of distinct trained immunity programs in human monocytes. *The Journal of clinical investigation*, (2022).
38. Netea MG, *et al.* Defining trained immunity and its role in health and disease. *Nat Rev Immunol* **20**, 375-388 (2020).
39. Ding C, *et al.* Inducing trained immunity in pro-metastatic macrophages to control tumor metastasis. *Nat Immunol* **24**, 239-254 (2023).

40. Geller AE, *et al.* The induction of peripheral trained immunity in the pancreas incites anti-tumor activity to control pancreatic cancer progression. *Nat Commun* **13**, 759 (2022).
41. Hamdan F, *et al.* Leveraging glucan-induced trained immunity for the epigenetic and metabolic rewiring of macrophages to enhance colorectal cancer vaccine response. *Nat Commun* **17**, 1757 (2026).
42. Bekkering S, Quintin J, Joosten LA, van der Meer JW, Netea MG, Riksen NP. Oxidized low-density lipoprotein induces long-term proinflammatory cytokine production and foam cell formation via epigenetic reprogramming of monocytes. *Arterioscler Thromb Vasc Biol* **34**, 1731-1738 (2014).
43. Keating ST, *et al.* Rewiring of glucose metabolism defines trained immunity induced by oxidized low-density lipoprotein. *J Mol Med (Berl)* **98**, 819-831 (2020).
44. Jie L, *et al.* High Mobility Group Protein B1 Promotes Interferon Regulatory Factor 1 SUMOylation to Prime Trained Immunity of Circulating Monocytes and Aggravate the Progressive Synovial Inflammation in Knee Osteoarthritis. *Research (Wash D C)* **9**, 1243 (2026).
45. Hajishengallis G, Chavakis T. Central trained immunity and its impact on chronic inflammatory and autoimmune diseases. *J Allergy Clin Immunol* **154**, 1113-1116 (2024).
46. Ochando J, Mulder WJM, Madsen JC, Netea MG, Duivenvoorden R. Trained immunity - basic concepts and contributions to immunopathology. *Nat Rev Nephrol* **19**, 23-37 (2023).
47. Zhang Z, Zhang Y, Lieberman J. Lighting a Fire: Can We Harness Pyroptosis to Ignite Antitumor Immunity? *Cancer Immunol Res* **9**, 2-7 (2021).
48. Liu X, Xia S, Zhang Z, Wu H, Lieberman J. Channelling inflammation: gasdermins in physiology and disease. *Nat Rev Drug Discov* **20**, 384-405 (2021).
49. Yu P, Zhang X, Liu N, Tang L, Peng C, Chen X. Pyroptosis: mechanisms and diseases. *Signal Transduct Target Ther* **6**, 128 (2021).
50. Wang Q, *et al.* A bioorthogonal system reveals antitumour immune function of pyroptosis. *Nature* **579**, 421-426 (2020).
51. Plitas G, *et al.* Regulatory T Cells Exhibit Distinct Features in Human Breast Cancer. *Immunity* **45**, 1122-1134 (2016).
52. Zheng P, *et al.* Neoantigen-Based Nanovaccine In Combination with Immune Checkpoint Inhibitors Abolish Postsurgical Tumor Recurrence and Metastasis. *Small*, e2302922 (2023).
53. Xi X, *et al.* Self-healing microcapsules synergetically modulate immunization microenvironments for potent cancer vaccination. *Sci Adv* **6**, eaay7735 (2020).
54. Liu Y, *et al.* A protease-cleavable liposome for co-delivery of anti-PD-L1 and doxorubicin for colon cancer therapy in mice. *Nat Commun* **16**, 2854 (2025).
55. Patsoukis N, Wang Q, Strauss L, Boussiotis VA. Revisiting the PD-1 pathway. *Sci Adv* **6**, (2020).

56. Maksymova L, Pilger YA, Nuhn L, Van Ginderachter JA. Nanobodies targeting the tumor microenvironment and their formulation as nanomedicines. *Mol Cancer* **24**, 65 (2025).
57. Broos K*, et al.* Non-invasive assessment of murine PD-L1 levels in syngeneic tumor models by nuclear imaging with nanobody tracers. *Oncotarget* **8**, 41932-41946 (2017).
58. Yang Y*, et al.* A personalized vaccine combining immunogenic cell death-induced cells and nanosized antigens for enhanced antitumor immunity. *Journal of controlled release : official journal of the Controlled Release Society* **376**, 1271-1287 (2024).
59. Tauriello DVF*, et al.* TGFβ drives immune evasion in genetically reconstituted colon cancer metastasis. *Nature* **554**, 538-543 (2018).
60. Watabe T, Takahashi K, Pietras K, Yoshimatsu Y. Roles of TGF-β signals in tumor microenvironment via regulation of the formation and plasticity of vascular system. *Semin Cancer Biol* **92**, 130-138 (2023).
61. Knopf P*, et al.* Acidosis-mediated increase in IFN-γ-induced PD-L1 expression on cancer cells as an immune escape mechanism in solid tumors. *Mol Cancer* **22**, 207 (2023).
62. Eris C, Zu C, Xiao Y, Platten M, Sun C. Regulation of immune checkpoint molecules in cancer immune evasion and therapy. *Nat Rev Cancer* **26**, 560-585 (2026).
63. Xu L*, et al.* Metabolic-epigenetic rewiring of CCR5(hi) monocytes sustains long-term trained immunity against lethal sepsis. *Sci Adv* **12**, eaee1634 (2026).
64. Chavakis T, Mitroulis I, Hajishengallis G. Hematopoietic progenitor cells as integrative hubs for adaptation to and fine-tuning of inflammation. *Nat Immunol* **20**, 802-811 (2019).
65. Zheng P*, et al.* Engineered Norovirus-Derived Nanoparticles as a Plug-and-Play Cancer Vaccine Platform. *ACS Nano*, (2023).

Supplementary Files

This is a list of supplementary files associated with this preprint. Click to download.

- SupplementaryInformation.pdf